Study of the Internal Dynamics of Molecules of Astrophysical Interest by Rotational Spectroscopy

by

Carolyn Gregory

A thesis submitted to the Faculty of Graduate Studies of

The University of Manitoba

in partial fulfilment of the requirements of the degree of

MASTER OF SCIENCE

Department of Chemistry

University of Manitoba

Winnipeg

Abstract

Molecules containing a methyl rotor can undergo internal rotation. The methyl's rotation relative to the molecule's frame leads to complicated splitting patterns in the rotational spectra, which are challenging to model and interpret. Researchers readily observe these splitting patterns using microwave spectroscopy, owing to the high resolutions obtainable in a collision-free environment. Still, molecules containing internal rotors have received less study due to their complexity. This research studied molecules that have complex internal dynamics. Specifically, two custom-built microwave spectrometers and high-level quantum chemical calculations enabled measurements and models of methyl cyanoacetate (MCA), 2-methyl-2-oxazoline (2M2O) and 2-ethyl-2-oxazoline (2E2O).

These molecules' spectra exhibit fine and hyperfine splittings due to the methyl rotor and the ^{14}N quadrupole nucleus. These were analyzed to derive their barriers to internal rotation. This research studied the effects of hyper-conjugative interactions on MCA's conformational stability and methyl barrier by comparing the derived barriers to those of similar molecules. For 2M2O and 2E2O, this work highlighted that the factors that govern the barriers in methylated molecules containing a partially unsaturated ring are poorly understood, as there has been little study on such molecules to date. As such, this work provides the basis for future studies on molecules with flexible ring systems containing a methyl rotor, which would aid our understanding of these types of molecules and the development of better computational models for analyzing and predicting their spectra.

Acknowledgements

I want to thank my supervisor, Dr. Jennifer van Wijngaarden, for being an incredibly patient mentor throughout my program. Through her guidance, I learned how much more goes into being a scientist than just science, and her dedication to her field continues to inspire me.

I also want to thank my advisory committee, Dr. Josh Hollett, Dr. Christian Kuss and Dr. Jason Morrison, for their kindness and enthusiasm for my research.

I would like to thank my current and former group members; Dr. Weslley G.D.P. Silva and Dr. Wenhao Sun for their guidance at the beginning of my program, and Tamanna Poonia, Joseph Stitsky and Rebecca Huard for creating an incredibly positive lab environment.

My deepest gratitude goes to my family and my partner for their unwavering support throughout my academic pursuits, without whom I could not have done this.

And finally, many thanks to the Faculty of Graduate Studies, the Faculty of Science and the Department of Chemistry for the financial support provided through scholarships, the University of Manitoba Graduate Fellowship and the SEGS program.

List of Tables

List of Figures

Table of Contents

Chapter 1 – Introduction

1.1. Interstellar Chemistry

The interstellar medium (ISM) is the region of space between planets, which are host to various conditions influenced by the stellar life cycle (Figure 1.1). New elements are formed by the fusion of stellar material in the first stages of a star's gravitational collapse and propelled outward into space by the shock waves accompanying this collapse. Low-mass stars form the more commonly found elements (e.g. C, N, O), while high-mass stars lead to supernovae and are responsible for creating heavier elements.[1,2]

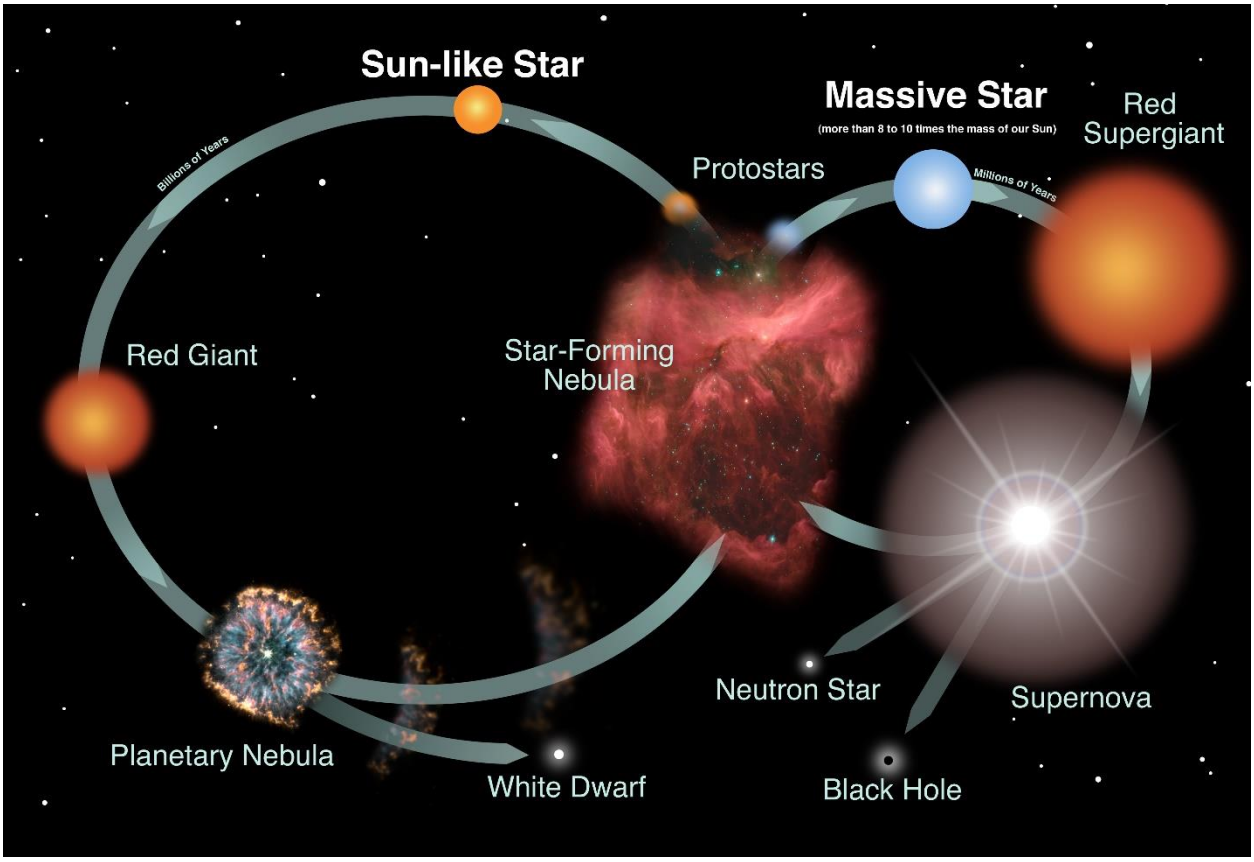

Figure 1.1. Diagram showing the lifecycles of Sun-like and massive stars. (Courtesy NASA/JPL-Caltech.)[3]

Nebulae are formed from the remnants of stellar death, cooling to temperatures of ~10 K and forming dense molecular clouds. Current theory posits that these clouds are the dominant source of complex chemistry in space that results from collisional reactions and surface-catalyzed reactions on interstellar ice and dust grains.[1,2]

Astrochemistry concerns itself with the discovery, classification, and reactions of molecular species in the interstellar medium. The majority of the 241 known different molecules detected in the ISM before 2021 have been discovered by radio astronomy and range in size from simple diatomic molecules to buckminsterfullerenes (C_{60}, C_{70}).[4]

Molecules with a strong dipole moment along one or more principal axes are easier to detect.[4] This is because the strength of detected transition signals from a molecule in rotational spectroscopy is related to the strength of the molecule's permanent dipole moment. Studying molecules with a weak or no dipole moment is possible using an analogue molecule with a single substitution of a more polar functional group to assess the likelihood of their presence in a given region of the ISM.[5] Commonly, the nitrile (C≡N) analogue of a molecule is a useful probe, owing to its large dipole moment which explains its prevalence in the ISM, with ~12% of the molecules already detected containing this functional group.[4] As a result, molecules having a nitrile group are strong candidates for detection in the ISM.

Several cyano-containing five- and six-membered cyclic molecules were recently detected in the dark molecular cloud TMC-1.[5] These are the first detections of five- and six-membered rings in any spectral region since the detection of benzene in 2001.[6] The detection of rings are of significant interest as these types of molecules form the foundational building blocks of biologically relevant molecules, including sugars. As such, there is a renewed interest in understanding the chemistry of these types of molecules in an astrophysical environment, as well as studying the spectra of other cyclic molecules, to facilitate future detections of these class compounds.[5]

With technological advancements like the Atacama Large Millimeter/submillimeter Array (ALMA) and the recently deployed James Webb Space Telescope, many more detections will be possible which will require the aid of laboratory experiments.

1.2. The Role of Laboratory Experiments in Astrochemistry

Laboratory experiments provide invaluable information that facilitates the identification of new species in the ISM and provides insight into the astrophysical processes that govern their environment.

An estimated 90%[4] of chemical species in the ISM have been detected using radio astronomy, which deals with spectra in the centimeter, millimeter and submillimeter wavelength ranges. As such, microwave and mm-wave spectroscopy are valuable techniques that can provide spectra for direct comparison with the spectra recorded by radio astronomers. These techniques utilize high-vacuum chambers and low rotational temperatures, which approximate conditions of common colder ISM regions.[7] Simulated rotational spectra based on quantum chemical calculations currently have a relative uncertainty of predicted line positions of 0.1% in the cm- and mm-wave regions and up to 0.2% in the submm-wave region.[8] These uncertainties can lead to predicted transitions being hundreds of MHz from their actual frequency. This level of uncertainty is manageable in a laboratory setting where the collected spectra are of isolated compounds or small mixtures of molecules. However, it is not well suited to discerning individual species in spectral line surveys obtained from astronomical spectra that may be populated with many hundreds of species. Thus, accurate experimental rotational parameters obtained from laboratory studies are crucial for making new identifications in the ISM but also provide the basis for eliminating transitions due to known species from congested astronomical spectra.

1.3. Methyl Rotors in the Interstellar Medium

To date, methyl-containing molecules make up ~13% of the molecules detected in the ISM.[4] Such molecules exhibit unique spectral properties due to the internal rotations of the methyl group, which can turn relative to the rest of the molecule. This rotation is hindered by a three-fold symmetric barrier which splits the energy levels into states of A and E symmetry. Depending on the size of the barrier, this can lead to splittings in high-resolution spectra. An example of a V_3 barrier for acetaldehyde is presented in Figure 1.2.

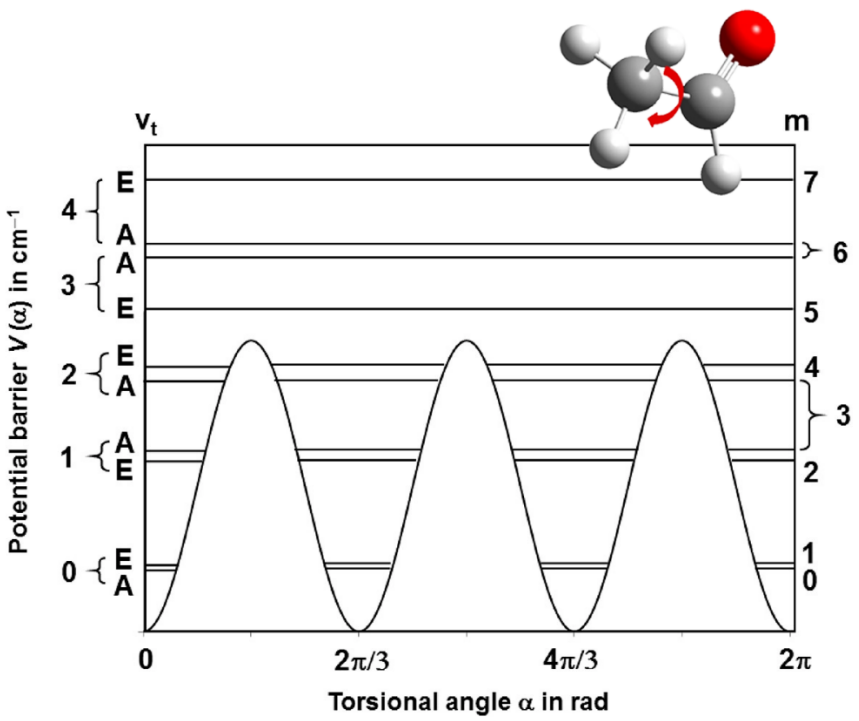

Figure 1.2. An example of a V_3 barrier for the internal rotation of the methyl group in acetaldehyde. Here, v_t is the principal torsional quantum number and m is the free-internal-rotor quantum number. Reproduced in part with permission from Kleiner (2019).[9]

As a result of the splittings, the spectra of molecules containing internal rotors are often dense, with as much as twice as many potentially observable rotational transitions. As previously indicated, computationally predicted transitions for any rotational species can have an error up to hundreds of MHz. Still, in the case of internal rotation, these discrepancies are even more pronounced. The degree of splitting between the two states is a function of the size of the barrier to internal rotation. Even minor errors in predictions of these barriers can lead to significant errors in the estimation of line positions for the two states.[10] The ability for calculations to accurately predict barriers for large-amplitude motions (LAMs), such as internal rotation can vary wildly based on the complexity of the theory used in the simulations, which further contributes to the uncertainty in correctly predicting line transitions for these molecules.[10]

Additionally, the properties of internal rotors, in particular the size and shape of the barriers to internal rotation, are sensitive to their chemical environment, and in the astrophysical context

can act as probes to study the interstellar medium.[9] Study of one of the simplest rotors, methanol, has allowed astronomers to use detections to analyze properties of the corresponding molecular clouds, such as densities and kinetic temperatures.[9] As a ubiquitous molecule in the ISM,[11] methanol which allows for a wide range of astrophysical environments to be studied. Methanol's rotation-torsion energies have also enabled the consistency of fundamental physical constants over time to be studied.[12]

Lastly, many biologically relevant molecules contain methyl rotors. As a fundamental goal of astrochemistry is to understand how these molecules arose in the interstellar medium, understanding methyl rotors and their properties will be crucial in understanding how they arise in the interstellar medium and how they interact with other molecular species to form these target molecules.

The work in this thesis investigates the rotational spectra of molecules of astrophysical interest with complex internal dynamics using microwave spectroscopy with the aid of quantum chemical calculations. An overview of the principles of rotational spectroscopy and internal rotation is included in Chapter 2. The experimental and computational details, including a description of the two custom-built microwave spectrometers in the van Wijngaarden lab, are given in Chapter 3. Chapter 4 presents a microwave study of methyl cyanoacetate, including a discussion on the intramolecular dynamics governing its conformational landscape and their effects on the V_3 barrier for the ground state conformer. Chapter 5 presents a study on two methylated derivatives of 2-oxazoline and includes a discussion of the significance of the composition of the ring surrounding the methyl substitution site. Finally, Chapter 6 summarizes the significant observations found through this work and presents further avenues of investigation.

1.4. References

(1) Chevance, M.; Kruijssen, J. M. D.; Vazquez-Semadeni, E.; Nakamura, F.; Klessen, R.; Ballesteros-Paredes, J.; Inutsuka, S. ichiro; Adamo, A.; Hennebelle, P. The Molecular Cloud Lifecycle. *Space Sci. Rev.* **2020**, *216* (4), 1–42.

(2) Gerin, M. The Molecular Universe. In *Astrochemistry and Astrobiology*; Smith, I. W. M., Cockell, C. S., Leach, S., Eds.; Springer Berlin Heidelberg: Berlin, Heidelberg, 2013; pp 35–72.

(3) *Lives of Stars Diagram / Periodic Table of Elements [Banner - SUPERNOVA Toolkit] | Night Sky Network*. https://nightsky.jpl.nasa.gov/download-view.cfm?Doc_ID=289 (accessed 2022-12-23).

(4) McGuire, B. A. 2021 Census of Interstellar, Circumstellar, Extragalactic, Protoplanetary Disk, and Exoplanetary Molecules. *Astrophys. J. Suppl. Ser.* **2022**, *259* (2), 30.

(5) McCarthy, M. C.; Mcguire, B. A. Aromatics and Cyclic Molecules in Molecular Clouds: A New Dimension of Interstellar Organic Chemistry. *J. Phys. Chem. A* **2021**, *125* (16), 3231–3243.

(6) Cernicharo, J.; Heras, A. M.; Tielens, A. G. G. M.; Pardo, J. R.; Herpin, F.; Guélin, M.; Waters, L. B. F. M. Infrared Space Observatory's Discovery of C4H2, C6H2, and Benzene in CRL 618. *Astrophys. J.* **2001**, *546* (2), L123.

(7) Savin, D. W.; Brickhouse, N. S.; Cowan, J. J.; Drake, R. P.; Federman, S. R.; Ferland, G. J.; Frank, A.; Gudipati, M. S.; Haxton, W. C.; Herbst, E.; Profumo, S.; Salama, F.; Ziurys, L. M.; Zweibel, E. G. The Impact of Recent Advances in Laboratory Astrophysics on Our Understanding of the Cosmos. *Reports Prog. Phys.* **2012**, *75* (3), 36901.

(8) Puzzarini, C.; Barone, V. The Challenging Playground of Astrochemistry: An Integrated Rotational Spectroscopy – Quantum Chemistry Strategy. *Phys. Chem. Chem. Phys.* **2020**, *22* (12), 6507–6523.

(9) Kleiner, I. Spectroscopy of Interstellar Internal Rotors: An Important Tool for Investigating Interstellar Chemistry. *ACS Earth Sp. Chem.* **2019**, *3* (9), 1812–1842.

(10) Nguyen, H. V. L.; Kleiner, I. Understanding (Coupled) Large Amplitude Motions: The Interplay of Microwave Spectroscopy, Spectral Modeling, and Quantum Chemistry. *Phys. Sci. Rev.* **2022**, *7* (6), 679–726.

(11) Liszt, H. S.; Pety, J.; Lucas, R. Limits on Chemical Complexity in Diffuse Clouds: Search for CH3OH and HC5N Absorption. *Astron. Astrophys.* **2008**, *486* (2), 493–496.

(12) Bagdonaite, J.; Jansen, P.; Henkel, C.; Bethlem, H. L.; Menten, K. M.; Ubachs, W. A Stringent Limit on a Drifting Proton-to-Electron Mass Ratio from Alcohol in the Early Universe. *Science* **2013**, *339* (6115), 46–48.

Chapter 2 – Rotational Spectroscopy

2.1. Introduction

Rotational spectroscopy focuses on transitions in the electromagnetic spectrum's microwave or cm-wave region, which correspond to a molecule's rotational transitions. Molecules which contain a permanent electric dipole moment can be studied by this technique, yielding highly accurate rotational and centrifugal distortion constants. As the rotational constants relate to the moments of inertia of the molecule, as will be discussed in this chapter, microwave spectroscopy is highly sensitive to the molecule's geometry, allowing for the distinction between varying conformations and isotopologues. Centrifugal distortion constants can additionally provide insight into the topology of the molecule's vibrational potential of a given vibrational motion. Additionally, microwave spectroscopy enables analysis of the effects of internal dynamics, such as internal rotation, which appear as splittings in the spectral peaks.

The remainder of this chapter contains a brief overview of general rotational spectroscopy theory[1–3] and internal rotation.[4–7] The interested reader is encouraged to read the detailed accounts in the references mentioned.

2.2. Moments of Inertia and Rotational Constants

Rotational spectroscopy interacts with each molecule through its moments of inertia. These moments relate to the masses of the atoms (m) in the molecule and the distances from the center of mass (r) to the inertial axes (a, b, c) of the molecule by

$$I_R = \sum m_i r_i^2 \qquad 2.1$$

where the subscript i represents the i^{th} atom in the molecule and $R = A, B, C$ denotes the inertial axes. As these parameters are specific to both the masses of the respective atoms and the arrangement of these atoms, the moments of inertia are sensitive to the geometry of the molecule in any given conformation. Thus, by analysis of the rotational spectra, the moments of inertia are obtained, which can infer molecular structures in an experiment and distinguish between different possible geometries a molecule can have.

Molecules can be classified with their moments of inertia along the principal rotational axes as follows:

1. Linear tops such as HCCH with $I_A = 0, I_B = I_C$.
2. Spherical tops such as P_4 with $I_A = I_B = I_C$.
3. Symmetric tops, which are further classified as prolate tops with $I_A < I_B = I_C$ such as molecules like CH_3CCH and oblate tops with $I_A = I_B < I_C$ such as C_6H_6.
4. Asymmetric tops, which make up most molecules, with $I_A < I_B < I_C$.

The rotational energy levels can be expressed by their term value *F(J)*, which differs based on the above classifications. For the linear top, which is the simplest case, its energy term value is given as

$$F(J) = BJ(J+1) \quad J = 0,1,2,\ldots \tag{2.2}$$

where *J* is the rotational quantum number and $B = \frac{h}{8\pi^2 I_B}$ is the rotational constant. Non-linear rotors will have three rotational constants which correspond to the three principal axes, i.e., $A = \frac{h}{8\pi^2 I_A}$, $B = \frac{h}{8\pi^2 I_B}$, and $C = \frac{h}{8\pi^2 I_C}$.

For a symmetric top rotor, there is an additional quantum number *K* representing the projection of the total rotational angular momentum quantum number *J* onto the highest symmetry axis. The term values differ for prolate and oblate symmetric tops, and their quantum number *K* takes on the subscripts K_a and K_c for prolate and oblate tops, respectively. Their term values are thus

$$F(J, K_a) = BJ(J+1) + (A-B)K_a^2 \quad J = 0,1,2,\ldots; \;\; K = 0, \pm 1, \pm 2, \ldots, \pm J \tag{2.3}$$

for prolate tops and

$$F(J, K_c) = BJ(J+1) + (C-B)K_c^2 \quad J = 0,1,2,\ldots; \;\; K = 0, \pm 1, \pm 2, \ldots, \pm J \tag{2.4}$$

for oblate tops.

Asymmetric top molecules are more complex, as their energy terms cannot be derived analytically from the Schrödinger equation, so their spectra are analyzed with respect to the prolate and oblate symmetric top limits, which can be seen in Figure 2.1. Their energy levels depend on three quantum labels $J_{K_a K_c}$, with K_a and K_c representing the prolate and oblate limits.

The asymmetry parameter κ is defined as

$$\kappa = \frac{2B - A - C}{A - C} \tag{2.5}$$

indicates the degree of asymmetry with

$$(\text{prolate case}) - 1 \leq \kappa \leq 1 \ (\text{oblate case}). \tag{2.6}$$

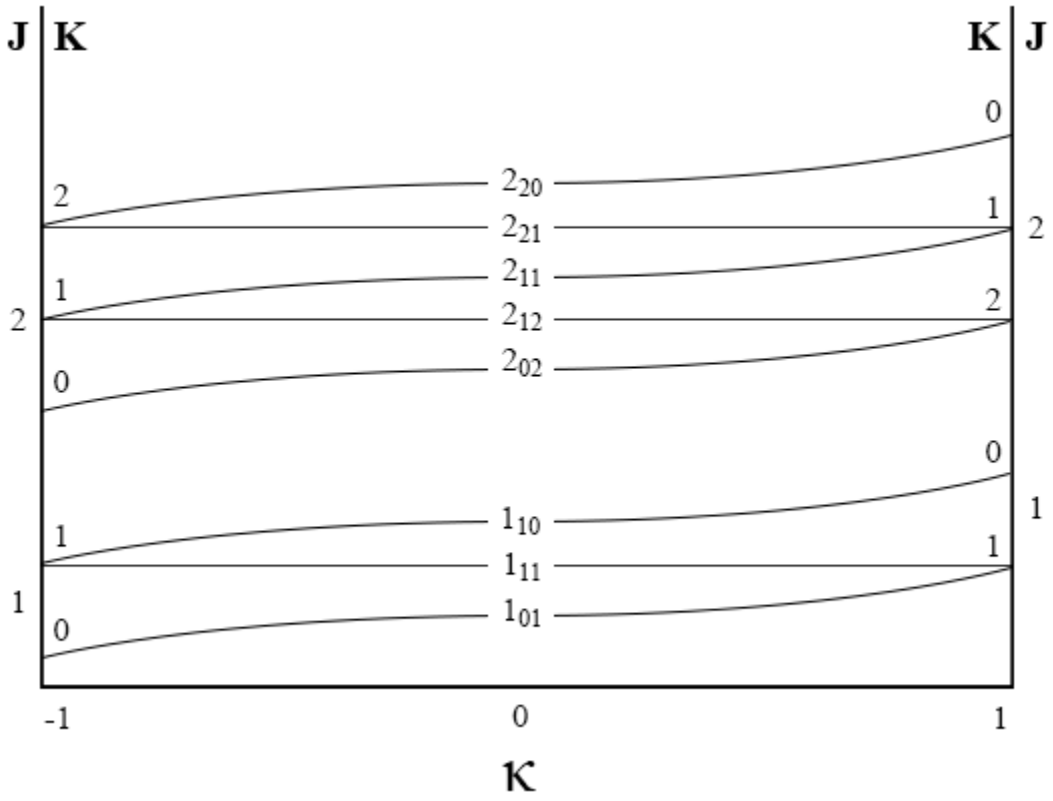

Figure 2.1. The labelling of the energy levels for an asymmetric top molecule produced by combining solutions for the prolate (κ = -1) and oblate (κ = 1) top limits.

For any classification, a given molecule must posses a non-zero dipole moment along any of the principal axes for a transition to be observed, with $\Delta J = 0, \pm 1$. Additionally, as there are three principal inertial axes, there are three types of transitions corresponding to these axes with additional selection rules, given as follows:

1. a-type transitions: $\mu_a \neq 0; \Delta K_a = \pm 2k$ and $\Delta K_c = \pm 2k +$ 1 for any integer k with the most intense transitions being those with $k = 0$.
2. b-type transitions: $\mu_b \neq 0; \Delta K_a = \pm 2k + 1$ and $\Delta K_c = \pm 2k + 1$ for any integer k.

3. *c*-type transitions: $\mu_c \neq 0; \Delta K_a = \pm 2k + 1$ and $\Delta K_c = \pm 2k$ for any integer k.

2.3. Centrifugal Distortion

The energy expressions in the previous sections were derived according to the rigid rotor model, i.e., that the geometry is unchanged by the effects of the rotation of the molecule. For lower rotational energy levels, this assumption is sometimes valid, but as the rotational energy increases, the effects of centrifugal forces acting on the atoms as the molecule rotates become more significant. As the rotational speed increases, the bond radii and angles change as a result of the centrifugal forces on the molecule as it rotates exerting an outward force on the atoms, resulting in a decrease in the energy difference between the rotational levels. Thus, additional terms are required to correct for the distortion effects that occur at higher J levels. For asymmetric tops, the quartic centrifugal distortion terms, namely Δ_J, Δ_{JK}, Δ_K, δ_J, and δ_K, are typically sufficient to describe these effects although higher order terms (sextic and beyond) are needed for highly distortable rotors.

2.4. Nuclear Quadrupole Interaction

Molecules containing an atom with a nuclear spin greater than ½ can exhibit splittings in their spectral peaks called hyperfine structure, the typical example being a molecule containing a ^{14}N atom which has a nuclear spin of 1. This specific type of hyperfine structure, termed nuclear quadrupole hyperfine structure, arises from the interaction of a non-spherical nuclear charge with the electric field gradient produced by the electrons. The coupling of the nuclear spin *I* and the molecular rotational angular momentum *J* is described by the quantum number *F*, which takes on the values $J + I, J + I - 1, J + I - 2, \ldots, |J - I|$ for molecules with a single quadrupolar nucleus. The energy levels are thusly labeled $J_{K_a K_c}F$. Additional selection rules for the hyperfine transitions are $\Delta F = 0, \pm 1$.

The molecules studied in this thesis all exhibit hyperfine structure from one ^{14}N quadrupole nucleus, along with fine structure due to the presence of an internal rotor, which will be discussed in the subsequent section.

2.5. Large-Amplitude Motions

Large-amplitude motions (LAMs) are internal motions in which a molecule can interconvert (or quantum mechanically tunnel) between equivalent conformations and lead to

splitting of the energy levels which gives rise to fine structure in the spectrum. There are many types of LAMs, including internal rotations of a symmetric (e.g., CH_3) or asymmetric (e.g., OH, NH_2) rotor, inversion tunnelling such as in the umbrella motion of NH_3, and pseudorotation and puckering in saturated ring systems. The properties of LAMs have been shown to be sensitive to the electronic structure of the molecule and are often poorly predicted by calculations, making them good probes for laboratory study of the internal dynamics of the molecule of interest and its potential energy surface. They can be studied by many methods, but due to its high spectral resolution, microwave spectroscopy is well suited for determining properties of LAMs, such as barrier heights to high degrees of accuracy.

The internal rotation of a methyl rotor is governed by a threefold potential which can be described as

$$V(\alpha) = \frac{V_3}{2}(1 - \cos 3\alpha) \qquad 2.7$$

where V_3 is the barrier to internal rotation and α is the angle of rotation of the methyl group, illustrated below in Figure 2.2. The rotational properties of the methyl rotor are described by its moment of inertia I_α and the rotational constant F_0.

The C_3 symmetry of the methyl rotor results in a characteristic splitting into two states, the A state and the doubly degenerate E state, where A and E are symmetry labels. The selection rules for the A and E states are that allowed transitions occur between energy states of the same symmetry, namely, A ↔ A, E ↔ E, A ↮ E. Typically, a larger V_3 barrier is associated with smaller splittings, with sufficiently high barriers (≥ 12 kJ mol^{-1}) exhibiting no splitting.

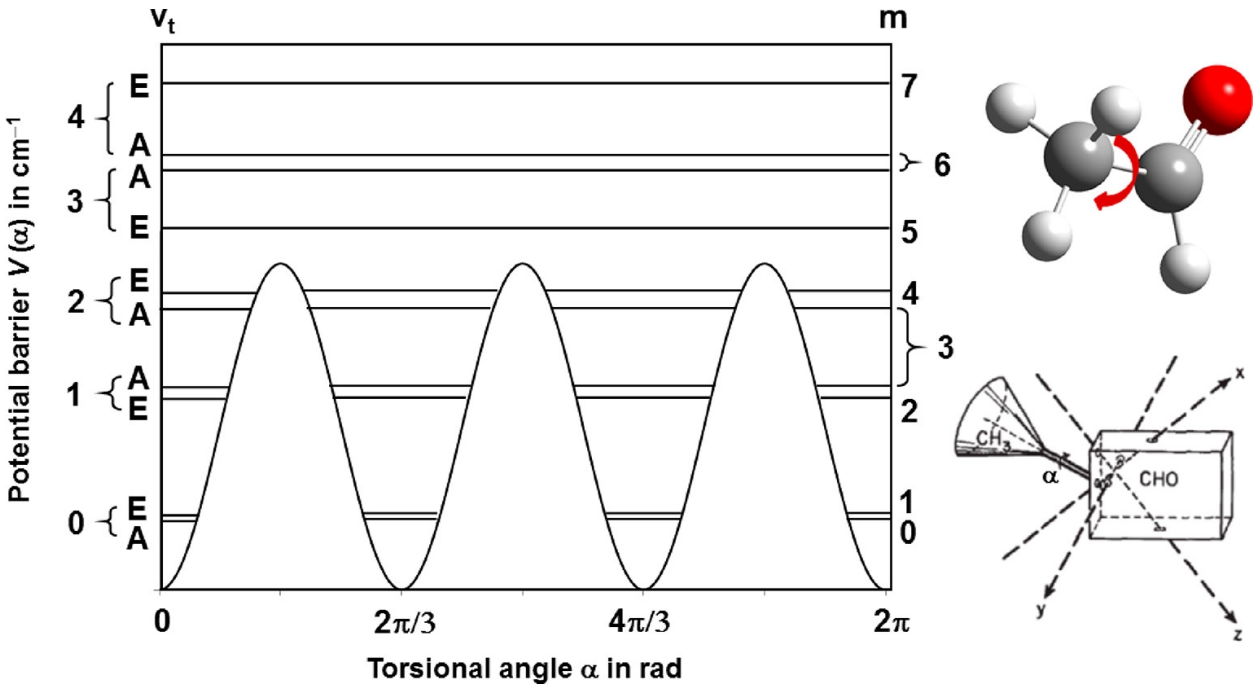

Figure 2.2. Potential energy barrier and axis system for acetaldehyde, with v_t representing the principal torsional quantum number and *m* the free-internal-rotor quantum number. Reproduced with permission from Kleiner (2019).[8]

For some molecules containing methyl rotors with V_3 barriers in the low to intermediate range, the geometry of the methyl rotor can experience centrifugal distortion effects in addition to the distortion effects present in the overall molecule in higher J states and thus require additional correction terms. The naming convention for these terms differs in different fitting programs, and as such in this work these will use the original notation described by Hansen *et al.*[9], namely, Dpi_{2J}, Dpi_{2K}, and Dpi_{2-}.

In studying the rotational spectra of molecules, we aim to discern the structure and internal dynamics of their molecular systems through the derivation of accurate spectroscopic parameters. Each molecule's potential energy surfaces define their system's dynamics, are unique to the geometry and provide insights into each system. The following chapter discusses the instrumentation of the custom-built microwave spectrometers used to obtain the spectra and the computational tools we use to aid in the interpretation of the spectra, thus facilitating a broader understanding of the molecules of interest.

2.7. References

(1) Gordy, W.; Cook, R. L. *Microwave Molecular Spectra*; John Wiley & Sons, Ltd: New York, 1984.

(2) Bernath, P. F. *Spectra of Atoms and Molecules*, 4th ed.; Oxford University Press: New York, 2020.

(3) Townes, C. H.; Schawlow, A. L. *Microwave Spectroscopy*, 2nd ed.; Dover Publications: Mineola, New York, 2012.

(4) Lin, C. C.; Swalen, J. D. Internal Rotation and Microwave Spectroscopy. *Rev. Mod. Phys.* **1959**, *31* (4), 841–891.

(5) Lister, D. G.; MacDonald, J. N.; Owen, N. L. *Internal Rotation and Inversion*; Academic Press Inc.: London, 1978.

(6) Kleiner, I. Asymmetric-Top Molecules Containing One Methyl-like Internal Rotor: Methods and Codes for Fitting and Predicting Spectra. *J. Mol. Spectrosc.* **2010**, *260* (1), 1–18.

(7) Nguyen, H. V. L.; Kleiner, I. Understanding (Coupled) Large Amplitude Motions: The Interplay of Microwave Spectroscopy, Spectral Modeling, and Quantum Chemistry. *Phys. Sci. Rev.* **2022**, *7* (6), 679–726.

(8) Kleiner, I. Spectroscopy of Interstellar Internal Rotors: An Important Tool for Investigating Interstellar Chemistry. *ACS Earth Sp. Chem.* **2019**, *3* (9), 1812–1842.

(9) Hansen, N.; Mäder, H.; Bruhn, T. A Molecular Beam Fourier Transform Microwave Study of 0-Tolunitrile: 14N Nuclear Quadrupole Coupling and Methyl Internal Rotation Effects. *Mol. Phys.* **1999**, *97* (4), 587–595.

Chapter 3 – Instrumentation and Computation

3.1. The Microwave Experiment

While each molecular species chosen for study presents its unique challenges, the approach to studying them is generalized as follows. A molecule is chosen for its chemical properties and purchased from a commercial supplier. Meanwhile, a series of quantum chemical calculations are conducted to determine the number of stable conformers and to estimate their rotational constants before measurement. Once the sample has arrived, the chirped pulse (cp) Fourier transform microwave (FTMW) spectrometer collects a survey scan using the initial estimates from species present and the spectral predictions of the calculated rotational constants. This survey scan is then analyzed to improve the accuracy of the rotational frequency estimates. The molecules are subsequently measured in the Balle-Flygare (bf) FTMW spectrometer using the improved estimates. These measurements provide accurate line positions and resolve any line splittings caused by the internal structure. Finally, the spectrum can be fit, and the experimentally determined spectroscopic parameters are derived.

The two custom-built FTMW instruments in the van Wijngaarden lab are different and used at different stages of the experimental process. However, their noteworthy commonalities are presented here for the sake of brevity. First, the liquid samples are placed in a bubbler, which is either used to form a 1% mixture in an inert carrier gas (typically neon) if the vapour pressure is sufficiently high or is in-line to bubble the carrier gas through it before its introduction into a 300 L stainless steel vacuum chamber. A pulsed solenoid nozzle with an orifice of 1 mm in diameter provides pulses of the sample into the chamber, where the pressure differential behind the nozzle ($\sim 10^{3}$ Torr) and the chamber ($\sim 10^{-6}$ Torr) forms a supersonic jet and cools the sample to rotational temperatures of ~2 K. A microwave excitation pulse is then broadcast into the chamber. If the molecules have rotational transitions corresponding to the frequency range of the pulse, the dipole moments of the molecular sample align with the polarizing pulse and macroscopically polarize the sample. After the pulse dissipates, the free induction decay (FID) signals corresponding to the loss of this polarization are detected in the time domain. These signals are then processed with a fast Fourier transform (FFT) to convert the spectra into the frequency domain.

3.2. Supersonic Jet Expansion

Supersonic jet expansion occurs in the FTMW spectrometers due to the carrier gas, the pressure differential between the sample inlet and the chamber, and the size of the orifice that separates the two.[1] The high pressure behind the nozzle and the small orifice ensures that many collisions will occur as the sample passes through the nozzle, wherein there is a transfer of energy from the molecular sample to the inert carrier gas which cools the rotational temperatures of the molecular sample to ~2 K. As the gas mixture undergoes adiabatic expansion, it accelerates due to the difference in pressure, and the mean velocity of the gas is much greater than the speed of sound. After a few mm of travel the gas mixture stops expanding because its molecules no longer collide and are moving at a uniform speed.

Sample introduction through supersonic expansion has many advantages. It allows for higher resolution peaks, as line broadening is virtually eliminated due to Doppler and pressure broadening. Additionally, the low rotational temperatures result in an enrichment of the lower rotational levels, which helps to reduce the complexity of the spectra. The low rotational temperatures can lead to the observation of fewer conformational species. This occurs when the barrier to interconversion between two conformers is low. In this case the higher energy conformer relaxes to the lower energy conformer and is not present in the resulting spectra.[2]

3.3. Chirped Pulse FTMW Spectrometer

The chirped pulse FTMW spectrometer[3,4] uses a broadband technique that allows the collection of a wide range of frequencies simultaneously in the range of 8-18 GHz. This is made possible by mixing a “chirp”, a rapid linear frequency sweep generated by an arbitrary waveform generator, with the continuous microwave radiation from a microwave synthesizer. The chirp can sweep a band of ±3 GHz around the center frequency. This allows recording of spectra in 6 GHz segments. The chirped microwave pulse is then amplified and broadcast into the vacuum chamber through a high gain horn antenna. At the same time, a pulsed solenoid valve delivers the sample perpendicularly to the direction of the excitation pulse. The microwave pulse polarizes the sample, and after it dissipates, a second high gain horn antenna located on the other side of the chamber detects the molecular emission. The resulting FIDs are then digitized by an oscilloscope after amplification and downconversion. The signal then undergoes an FFT to convert the spectrum to the frequency domain. A 10 MHz Rubidium standard is the reference clock for all the timing events

in the experiment, which results in phase coherent FIDs suitable for averaging together to reduce the signal-to-noise ratio of the time domain signal before FFT. Often, single spectra are each the result of averaging millions of FIDs. The schematic provided in Figure 3.1 illustrates the cp-FTMW spectrometer.

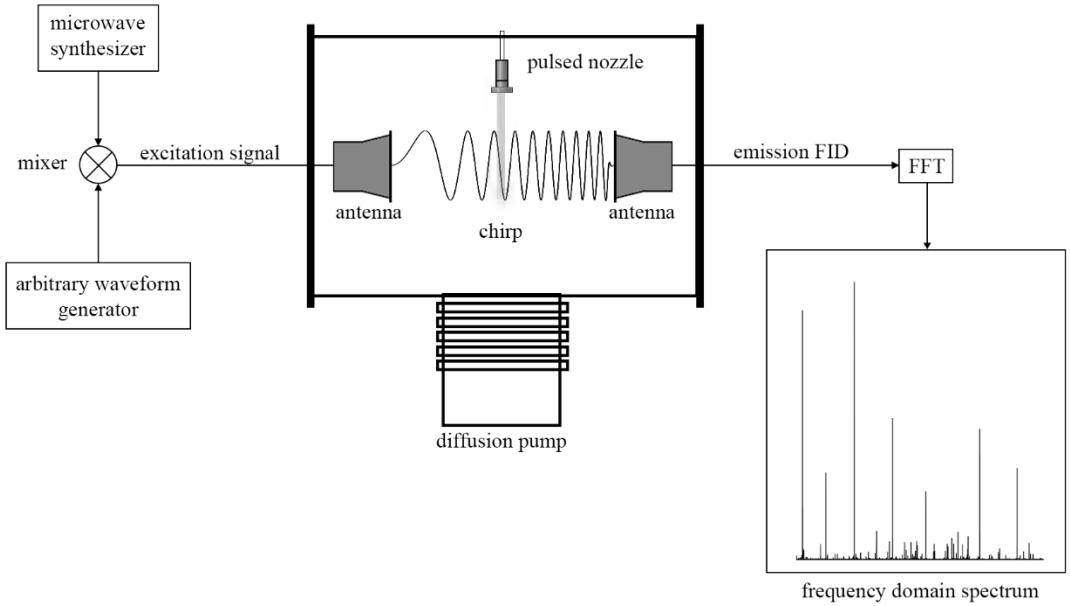

Figure 3.1. A simplified schematic of the cp-FTMW spectrometer. Further detail can be found in reference 3.

The essential advantage of the cp-FTMW spectrometer is in its efficiency, as the collection of spectra for a given study over the entire spectral range of the instrument can be completed in a few days' time. The speed comes at the cost of the resolving power found in the companion technique described in the next section. This lack of resolution results in typical linewidths of 200 kHz, which does not resolve line splitting due to nuclear quadrupole coupling or internal rotation. However, this method allows for spectral patterns to be identified rapidly, including initial assignments of conformers or minor isotopologues that may be present, making this technique an ideal starting point for investigating a species.

3.4. Balle-Flygare FTMW Spectrometer

The Balle-Flygare FTMW spectrometer[5,6] is a narrowband (< 1 MHz) instrument that collects high resolution spectra of individual rotational transitions and operates in a frequency

range of 4-26 GHz. The high resolution is possible because of a Fabry-Pérot cavity, which consists of two spherical concave mirrors with a variable separation of approximately 70 cm built within the vacuum chamber. One of the mirrors is fixed in place while a servo motor is affixed to the other, allowing operators to tune the distance between them to a given frequency. When tuned, the cavity forms a resonator and traps the microwave signal. An L-shaped wire hook antenna in the stationary mirror connected to a diode detector can verify the cavity's resonance, while a second antenna in the movable mirror is used to broadcast the excitation signals and receive the emission signals from the molecules. A simplified circuit diagram is given in Figure 3.2 and is described below.

The sample is introduced by a pulsed solenoid nozzle which is mounted slightly below the center of the movable mirror. An excitation signal is produced by mixing a continuous-wave signal generated by a microwave synthesizer with the output of a radiofrequency generator, which is broadcast to the sample via the L-shaped antenna in the movable mirror, while two single pole, double throw (SPDT) switches are used to generate an excitation pulse and protect the detection circuit from the pulse. Once the excitation pulse is complete, the detection circuit is activated via the same SPDT switches, and the transient emission signal is amplified and downconverted prior to digitization. An FFT is then used to convert the time-domain signal into the frequency domain. The signal appears as a Doppler doublet due to the coaxial arrangement of the nozzle with the microwave pulse. As the pulse timings in the experiment are all referenced to a 10 MHz system clock produced by the radiofrequency generator, the resulting signals are phase coherent and can be co-added to enhance the signal-to-noise ratio of the emission signal.

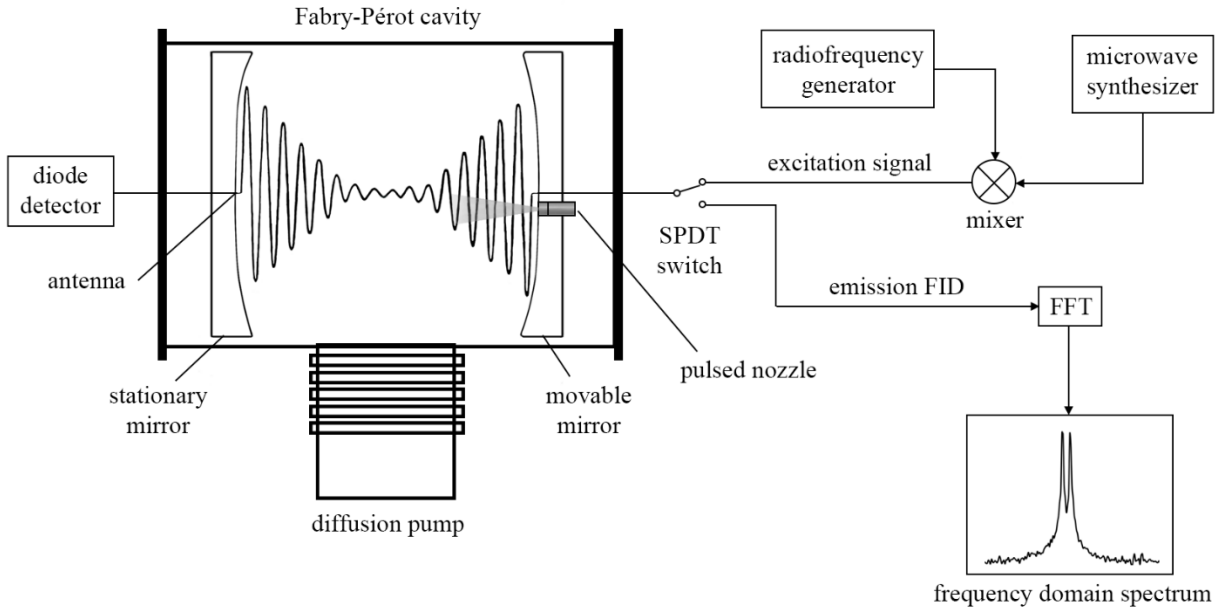

Figure 3.2. A simplified circuit diagram of the bf-FTMW spectrometer. This instrument is described in more detail in reference 5.

The linewidths using this technique (~7 kHz FWHM) are superior to that of the cp-FTMW, but the narrow bandwidth results in an emission spectrum with a ~1 MHz window, and as such collecting spectra for each transition in the range of the instrument is time-consuming, taking weeks or even months to collect what could be collected on the cp-FTMW in a matter of days. The high resolution of the bf-FTMW is necessary, however, to resolve the complex peak splittings that occur due to internal effects such as those discussed in this work.

3.5. Computational Methods

Computational chemistry is used at every stage of the experiment to aid in the understanding of the properties of the species of interest. Quantum chemical calculations performed using Gaussian 16[7] are done to obtain optimized geometries, probe the potential energy surface (PES) of the molecule, and predict rotational constants for all potential conformers. In this thesis, these calculations were conducted using MP2[8] and density functional theory (DFT) methods such as B3LYP-D3(BJ)[9–11] with Dunning's aug-cc-pVTZ[12] basis set.

For molecules with at least one rotatable bond, it is necessary to determine how many geometric configurations are possible.

When there are only one or two rotatable bonds, this can be accomplished using a series of single point energy calculations in a relaxed geometry scan in which a variable, in this case the dihedral angle of the rotatable group in relation to the frame of the molecule, is stepped incrementally while allowing for a full geometry optimization to be performed at each point. The relative energy at each point can then be plotted to identify possible geometric arrangements that correspond to a minimum on the potential energy surface. The geometries that correspond to any minima are then re-optimized and verified to be true minima using vibrational frequency analyses. An estimation of the rotational constants for any given conformer is obtained from the results of the geometry optimizations. The predicted constants are used in tandem with open-source spectral fitting software[13–15] to generate predicted spectra and as a first guess to fit the corresponding transitions that are measured experimentally.

If necessary, further quantum chemical calculations are conducted to rationalize what is observed experimentally. This includes non-covalent interaction (NCI)[16] analysis to calculate attractive and repulsive intramolecular forces that contribute to the relative stability of one conformation over another. Also used are natural bond orbital (NBO)[17] calculations to analyze orbital interactions.

The following chapters utilize the methods described herein to study the internal dynamics of several molecules containing a methyl rotor, for which the high resolution of the instruments allowed the identification of the complex splitting patterns that resulted.

3.6. References

(1) Smalley, R. E.; Wharton, L.; Levy, D. H. Molecular Optical Spectroscopy with Supersonic Beams and Jets. *Acc. Chem. Res.* **1977**, *10* (4), 139–145.

(2) Ruoff, R. S.; Klots, T. D.; Emilsson, T.; Gutowsky, H. S. Relaxation of Conformers and Isomers in Seeded Supersonic Jets of Inert Gases. *J. Chem. Phys.* **1990**, *93* (5), 3142–3150.

(3) Evangelisti, L.; Sedo, G.; Van Wijngaarden, J. Rotational Spectrum of 1,1,1-Trifluoro-2-Butanone Using Chirped-Pulse Fourier Transform Microwave Spectroscopy. *J. Phys. Chem. A* **2011**, *115* (5), 685–690.

(4) Brown, G. G.; Dian, B. C.; Douglass, K. O.; Geyer, S. M.; Shipman, S. T.; Pate, B. H. A

Broadband Fourier Transform Microwave Spectrometer Based on Chirped Pulse Excitation. *Rev. Sci. Instrum.* **2008**, *79* (5), 53103.

(5) Evangelisti, L.; Grabowiecki, A.; Van Wijngaarden, J. Chirped Pulse Fourier Transform Microwave Study of 2,2,2-Trifluoroethyl Formate. *J. Phys. Chem. A* **2011**, *115* (30), 8488–8492.

(6) Balle, T. J.; Flygare, W. H. Fabry–Perot Cavity Pulsed Fourier Transform Microwave Spectrometer with a Pulsed Nozzle Particle Source. *Rev. Sci. Instrum.* **1981**, *52* (1), 33–45.

(7) Frisch, M. J.; Trucks, G. W.; Schlegel, H. B.; Scuseria, G. E.; Robb, M. a.; Cheeseman, J. R.; Scalmani, G.; Barone, V.; Petersson, G. a.; Nakatsuji, H.; Li, X.; Caricato, M.; Marenich, a. V.; Bloino, J.; Janesko, B. G.; Gomperts, R.; Mennucci, B.; Hratchian, H. P.; Ortiz, J. V.; Izmaylov, a. F.; Sonnenberg, J. L.; Williams; Ding, F.; Lipparini, F.; Egidi, F.; Goings, J.; Peng, B.; Petrone, A.; Henderson, T.; Ranasinghe, D.; Zakrzewski, V. G.; Gao, J.; Rega, N.; Zheng, G.; Liang, W.; Hada, M.; Ehara, M.; Toyota, K.; Fukuda, R.; Hasegawa, J.; Ishida, M.; Nakajima, T.; Honda, Y.; Kitao, O.; Nakai, H.; Vreven, T.; Throssell, K.; Montgomery Jr., J. a.; Peralta, J. E.; Ogliaro, F.; Bearpark, M. J.; Heyd, J. J.; Brothers, E. N.; Kudin, K. N.; Staroverov, V. N.; Keith, T. a.; Kobayashi, R.; Normand, J.; Raghavachari, K.; Rendell, a. P.; Burant, J. C.; Iyengar, S. S.; Tomasi, J.; Cossi, M.; Millam, J. M.; Klene, M.; Adamo, C.; Cammi, R.; Ochterski, J. W.; Martin, R. L.; Morokuma, K.; Farkas, O.; Foresman, J. B.; Fox, D. J. Gaussian 16 Revision C.01. Gaussian Inc.: Wallingford CT 2016.

(8) Møller, C.; Plesset, M. S. Note on an Approximation Treatment for Many-Electron Systems. *Phys. Rev.* **1934**, *46* (7), 618–622.

(9) Becke, A. D. Density-functional Thermochemistry. III. The Role of Exact Exchange. *J. Chem. Phys.* **1993**, *98* (7), 5648–5652.

(10) Grimme, S.; Antony, J.; Ehrlich, S.; Krieg, H. A Consistent and Accurate Ab Initio Parametrization of Density Functional Dispersion Correction (DFT-D) for the 94 Elements H-Pu. *J. Chem. Phys.* **2010**, *132* (15), 154104.

(11) Grimme, S.; Ehrlich, S.; Goerigk, L. Effect of the Damping Function in Dispersion

Corrected Density Functional Theory. *J. Comput. Chem.* **2011**, *32* (7), 1456–1465.

(12) Dunning, T. H. Gaussian Basis Sets for Use in Correlated Molecular Calculations. I. The Atoms Boron through Neon and Hydrogen. *J. Chem. Phys.* **1989**, *90* (2), 1007–1023.

(13) Western, C. M. PGOPHER: A Program for Simulating Rotational, Vibrational and Electronic Spectra. *J. Quant. Spectrosc. Radiat. Transf.* **2017**, *186*, 221–242.

(14) Hartwig, H.; Dreizler, H. The Microwave Spectrum of Trans-2,3-Dimethyloxirane in Torsional Excited States. *Zeitschrift für Naturforsch. A* **1996**, *51* (8), 923–932.

(15) Hansen, N.; MÄDER, H.; Bruhn, T. A Molecular Beam Fourier Transform Microwave Study of 0-Tolunitrile: 14N Nuclear Quadrupole Coupling and Methyl Internal Rotation Effects. *Mol. Phys.* **1999**, *97* (4), 587–595.

(16) Johnson, E. R.; Keinan, S.; Mori-Sánchez, P.; Contreras-García, J.; Cohen, A. J.; Yang, W. Revealing Noncovalent Interactions. *J. Am. Chem. Soc.* **2010**, *132* (18), 6498–6506.

(17) Weinhold, F.; Landis, C. R.; Glendening, E. D. What Is NBO Analysis and How Is It Useful? *Int. Rev. Phys. Chem.* **2016**, *35* (3), 399–440.

Chapter 4 – Methyl Cyanoacetate

Contribution of Authors

The content of this chapter is an adapted version of an article published in the Journal of Molecular Spectroscopy under the citation: Gregory, C.; Silva, W.G.D.P.; van Wijngaarden, J. Rotational Spectrum and Quantum Chemical Calculations of Methyl Cyanoacetate: A Compound of Potential Astrochemical Interest. *J. Mol. Spectrosc.* **2021**, *377*, 1–7.

Author contributions:

1. Carolyn Gregory – Conceptualization, collection and assignment of experimental spectrum, performed calculations, contributed writing to original draft.
2. Weslley G.D.P. Silva – Performed and interpreted NBO-del/NCI calculations, contributed writing to original draft.
3. Jennifer van Wijngaarden – Contributed writing to original draft.

4.1. Introduction

Methyl cyanoacetate ($H_3CO(CO)CH_2CN$) (MCA) was chosen to study as a candidate for future astronomical searches owing to the prevalence of cyano-containing species in the ISM and the detection of methyl acetate ($H_3CO(CO)CH_3$) in Orion in 2013.[1] No prior studies of the pure rotational spectrum of MCA have been conducted in any spectral region. In contrast, its vibrational spectrum has been extensively studied in gas-phase,[2] solution,[2–4] liquid,[2,3,5–7] and crystalline[2,3,5] forms as well as using matrix isolation techniques.[8,9] These previous studies, some aided by theoretical studies,[2,4,6–10] indicate that MCA can take on four possible geometric arrangements through the rotation about the single bond within the ester fragment (H_3CO-C=O) and about the single bond which governs the orientation of the terminal cyano group (O=C-CH_2CN). The methyl group of the ester fragment can adopt a *syn* or *anti* arrangement with respect to the carbonyl group, though the *syn* conformation was calculated to be more stable by ~45 kJ mol^{-1} (HF/6-31G*).[7] The orientation of the cyano fragment relative to the carbonyl, assuming a *syn* orientation of the ester moiety, has been found to be either *syn* or *gauche* relative to the carbonyl group.[2–9] The theoretical components of these studies indicate that the energy difference between these two conformers is relatively small, ranging from 0.174 kJ mol^{-1} [8] – 3.92 kJ mol^{-1},[2] with most predicting that the *syn* conformer is the most stable.[2,4,6–9] The energy ordering from the theoretical calculations was used to guide the interpretation of the experimental IR and Raman spectra, for which spectral features

of only the *syn* form or a mixture of the *syn/gauche* conformers were identified depending on sample phase and temperature. Higher level calculations (B3LYP/6-31++G(d,p)), however, indicate that the *gauche* form is not a minimum, but a transition state, with the two minima occurring when the cyano fragment is *syn* or *anti* with respect to the carbonyl, with the *anti* form more stable by 1.10 kJ mol^{-1}.[10]

Given the discrepancies in the experimental and theoretical results which support a (O=C-C-C) dihedral angle between 110°[6] and 180°[10] (with most ~140-145°)[2,7,8] and with the disagreement between whether this conformer is more or less stable than the *syn* orientation, additional investigation was undertaken. This study employed the use of high-level quantum chemical calculations (B3LYP-D3(BJ)/aug-cc-pVTZ) along with microwave spectroscopy to conclusively determine the ground state geometry as well as to obtain the rotational spectroscopic parameters of conformer I and those related to the internal methyl rotor by resolving splittings arising from the ^{14}N quadrupole nucleus and the A/E splitting due to the rotor. Additional calculations were used to rationalize the energy ordering of the four possible conformers of MCA, namely natural bond orbital (NBO) and non-covalent interaction (NCI) calculations. With the most stable form unambiguously confirmed, this study forms the basis for a future identification of MCA in the ISM.

4.2. Computational Methods

A two-dimensional potential energy surface (PES) of MCA was derived at the B3LYP-D3(BJ)/cc-pVTZ level of theory by stepping the two rotatable bonds (θ and ϕ, see Figure 4.1) in 10° increments and obtaining a single point energy calculation at each point, allowing all other parameters to relax. The PES, shown in Figure 4.1, indicated the presence of four unique minima, two low-energy structures with the angle θ = 0° which corresponds with the O-CH_3 bond oriented *syn* to the carbonyl group and two much higher energy forms in which θ = 180° (anti). Two of the minima, where ϕ ≠ 0°, were found to have mirror images, with ϕ = ±170° for the low energy (θ = 0°) conformer and ϕ = ±115° for the high energy conformer.

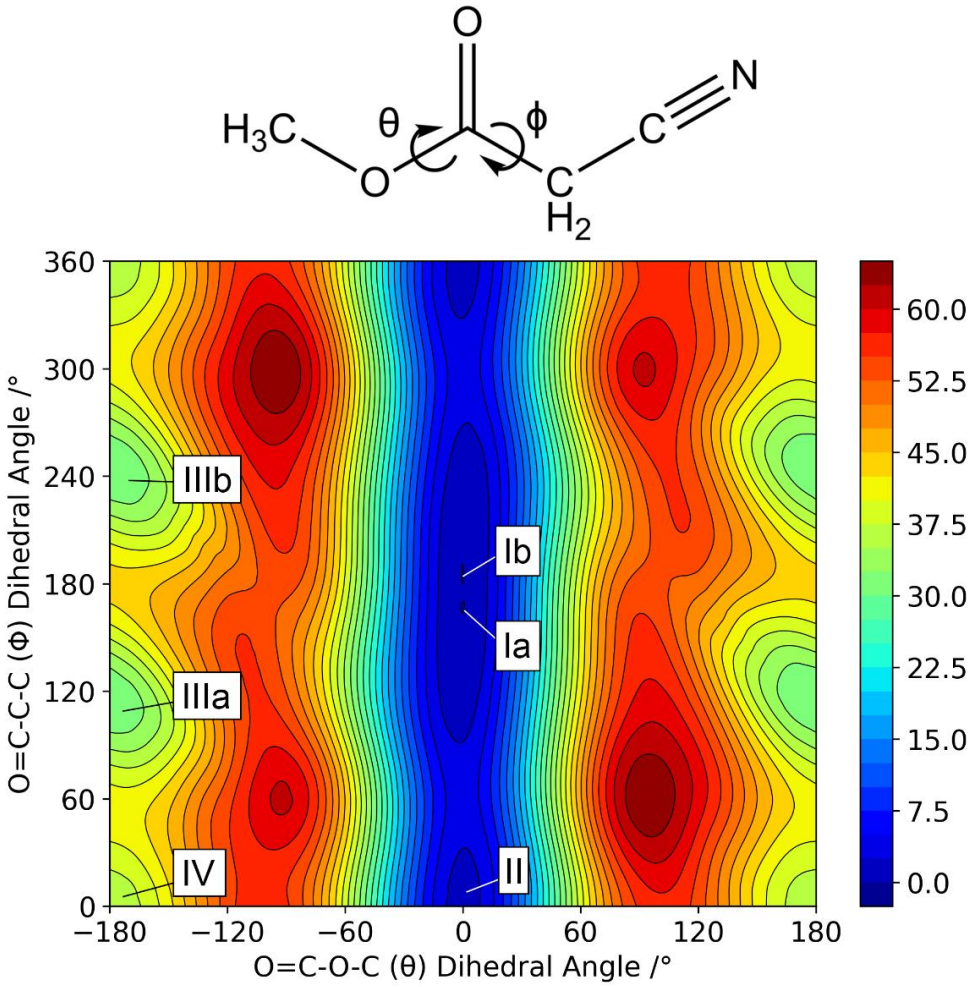

Figure 4.1. Potential energy surface of MCA calculated at the B3LYP-D3(BJ)/cc-pVTZ level of theory as a function of dihedral angles θ and ϕ defined above. The colour gradient represents the relative energy in kJ mol^{-1}. Minima correspond to four unique conformers with the enantiomer pair Ia/Ib defined as the global minimum geometry.

The structures identified in the PES were reoptimized at the B3LYP-D3(BJ)/aug-cc-pVTZ level of theory along with harmonic frequency analyses at the same level of theory, where the resulting structures (Figure 4.2) were confirmed to be true minima. These calculations also yielded estimated rotational constants, dipole moments, and zero point corrected relative energies for each conformer, which are shown in Table 4.1.

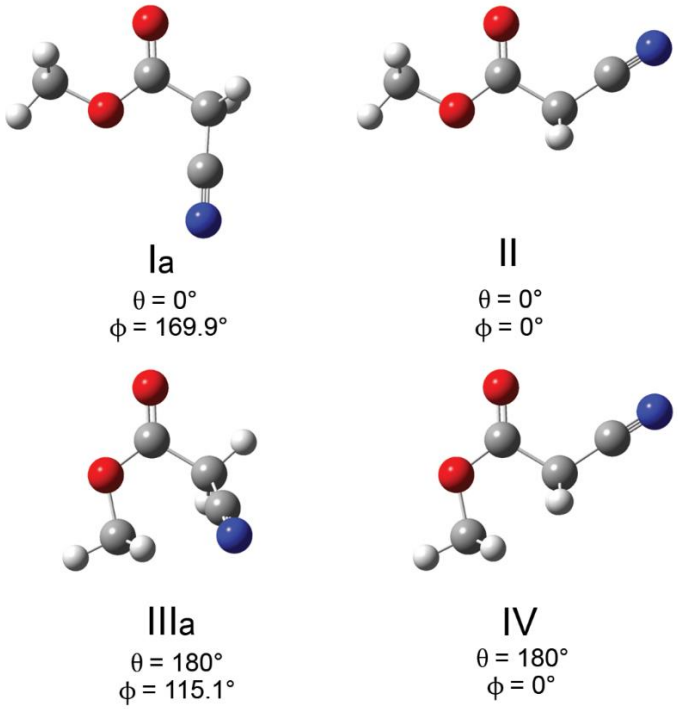

Figure 4.2. Possible geometries of MCA optimized at the B3LYP-D3(BJ)/aug-cc-pVTZ level of theory. Conformers I and III both have a mirror image where ϕ = 190.1° for Ib and ϕ = 244.9° for IIIb.

Table 4.1. Calculated spectroscopic parameters for the conformers of MCA obtained at the B3LYP-D3(BJ)/aug-cc-pVTZ level of theory.

		Conformer Ia/b	Conformer II	Conformer IIIa/b	Conformer IV
A	/MHz	5068	9525	3770	6225
B		1839	1406	2265	1626
C		1376	1244	1595	1310
μ_a	/Debye	2.34	4.62	0.21	4.86
μ_b		0.60	3.12	2.06	4.80
μ_c		0.45	0.00	3.33	0.00
Energy [a]	/kJ mol^{-1}	0	1.4	29.8	34.8
Population [b]		63.9%	36.1%	0.0%	0.0%

[a] Relative zero-point energy corrected. [b] Boltzmann population at 298 K.

Additional scans were conducted at both the B3LYP-D3(BJ) and MP2 levels of theory using the aug-cc-pVTZ basis set to visualize the relaxation pathway between the two most stable conformers of MCA by stepping the angle ϕ in 20 increments of 10°, given in Figure 4.3. Scans of the methyl rotor for the two lower energy conformers were done similarly by stepping the C-O-C-H dihedral to determine the barrier to internal rotation, shown in Figure 4.4.

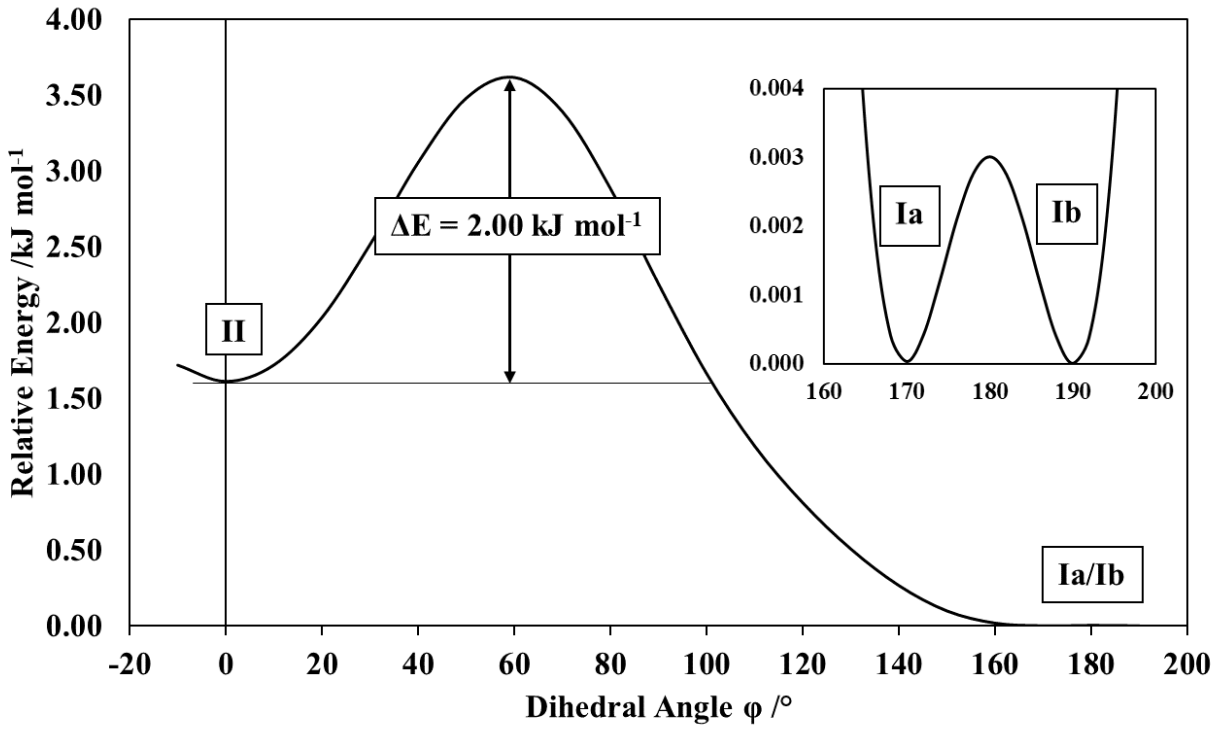

Figure 4.3. Potential energy curve for the interconversion of conformers I and II of MCA calculated at the B3LYP-D3(BJ)/aug-cc-pVTZ level of theory. The inset shows the details around minima at 169.9° and 190.1° corresponding to conformers Ia and Ib.

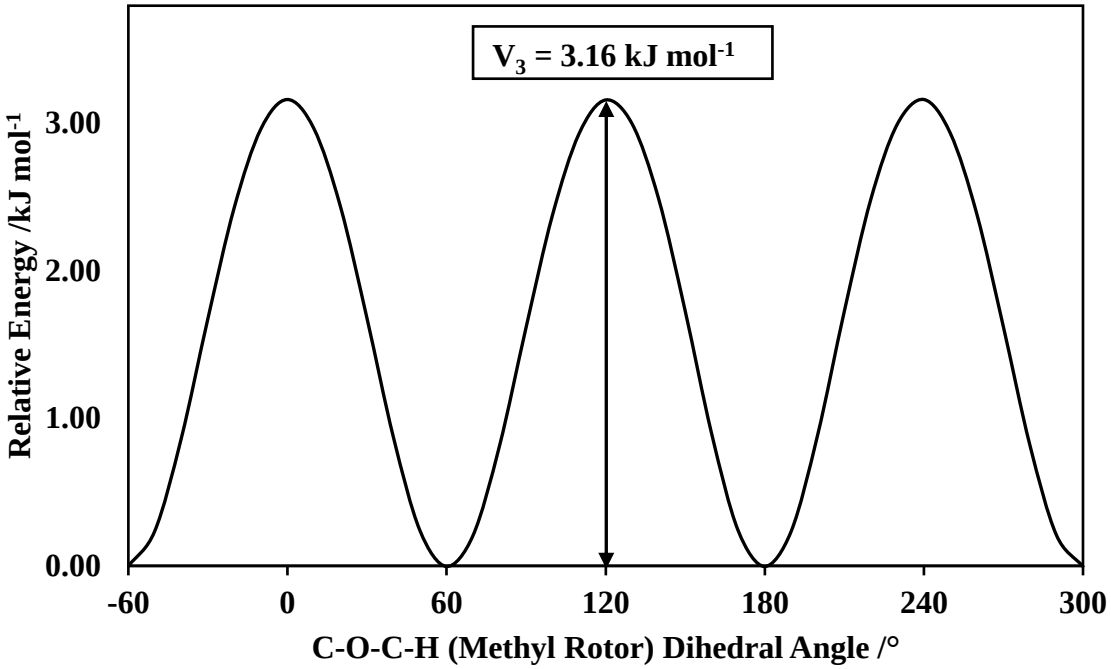

Figure 4.4. Potential energy curve for the methyl internal rotation of conformer I calculated at the B3LYP-D3(BJ)/aug-cc-pVTZ level of theory, where 0° is referenced to the H atom *antiperiplanar* to the carbonyl group.

For the two most stable conformers of MCA, a non-covalent interaction (NCI) analysis was performed using the NCIPLOT program to visualize the intramolecular interactions present in each conformer. For all conformers, natural bond orbital (NBO) calculations including deletion of all antibonding and Rydberg-type orbitals were conducted using the NBO 7.0 program at the B3LYP-D3(BJ)/aug-cc-pVTZ level of theory to determine the second-order perturbation energies which correspond to different charge transfer interactions and to differentiate between the Lewis (steric/electrostatic interactions) and non-Lewis (hyperconjugation) contributions to the full electronic energy.

4.3. Experimental

Methyl cyanoacetate (99%) was purchased from Alfa Aesar and used without further purification. The sample is liquid at room temperature (m.p. -23°C) but is not particularly volatile (b.p. 204°C), so to facilitate its conversion to the gas phase, ~2 mL of sample was placed in a stainless steel reservoir (½" internal diameter) seated in a band heater and mounted in the vacuum

chamber ~10 cm upstream from a General Valve Series 9 pulsed nozzle with a 1 mm diameter orifice, where it was heated to ~80°C prior to the introduction of the inert carrier gas (neon) before the expansion. The rotational spectrum of MCA was collected using both instruments described in Chapter 3.

4.4. Spectral Analysis

While four conformers of MCA were predicted by the calculations (Table 4.1), only conformers I and II are expected to be readily populated at room temperature. Conformer I is predicted to be more stable by 1.4 kJ mol^{-1}, corresponding to a relative Boltzmann population of 64% at room temperature, or approximately 62% at 80°C (the temperature of the liquid sample) where conformer II is slightly enriched. The dihedral scans (Figure 4.1 and Figure 4.3) indicate that conformer I is an enantiomeric pair, with the terminal cyano group rotated out of the plane of the backbone by ±10.1°, corresponding with minima at φ = 169.9° and 190.1°. The conversion pathway between Ia/Ib is plotted in the inset of Figure 4.3, which is essentially barrierless at both B3LYP-D3(BJ) and MP2 levels of theory using the aug-cc-pVTZ basis set, as the zero-point energy was found to lie above the transition state at ϕ = 180°, implying that a large-amplitude motion about the φ angle is present.

From the estimated spectral parameters calculated in Table 4.1, the ground state rotational spectrum of conformer I should exhibit strong *a*-type patterns. The predicted spectrum was simulated using the PGOPHER[11] software and the most intense lines in the experimental broadband spectrum were readily assigned to conformer I. This assignment was further supported by the observation of less intense *b*-type transitions. While there is a non-zero predicted μ_c dipole moment (0.45 D), no *c*-type transitions were observed, which is consistent with a barrierless interconversion between the Ia/Ib minima on the PES that averages this contribution to zero.

Higher resolution measurements on the bf-FTMW spectrometer revealed complex splitting patterns owing to both the ^{14}N quadrupole nucleus and the A/E splitting of the methyl internal rotor, with an example of a strong *a*-type transition shown in Figure 4.5.

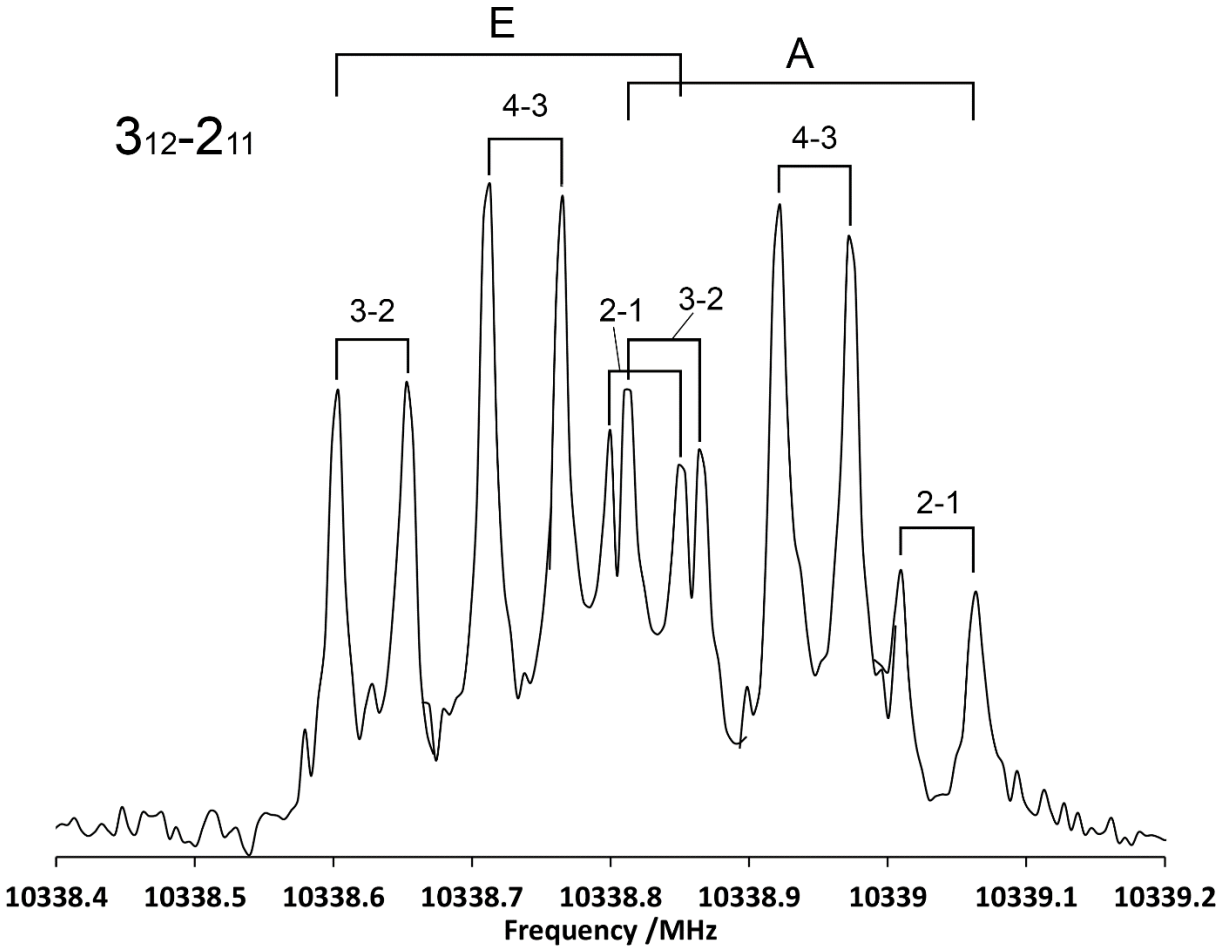

Figure 4.5. Sample Balle-Flygare spectrum detailing the splitting patterns due to the ^{14}N hyperfine structure and the internal rotation of the methyl group for a single rotational transition. The labels are for the F'- F" quadrupole hyperfine components. Note that this spectrum comprises smaller segments collected with different excitation frequencies, each averaging 50 cycles.

The XIAM program[12] was used to fit the A and E states simultaneously, which allowed for the determination of the V_3 barrier, the angle between the rotor α-axis and the principal inertial a-axis of the molecule (δ), the rotational constant of the methyl top (F_0), as well as the rotational, quartic centrifugal distortion and ^{14}N quadrupole coupling constants, all of which are summarized in Table 4.2. The centrifugal distortion constant D_K was not well-determined in the fit and thus was fixed to the theoretical value, resulting in a fit of 153 lines with a rms standard deviation of 2.4 kHz.

Table 4.2. Spectroscopic parameters for conformer I of MCA.[a]

		XIAM	B3LYP-D3(BJ)/ aug-cc-pVTZ	MP2/ aug-cc-pVTZ
A	/MHz	5069.2803(10)	5068	5083
B		1842.95524(23)	1839	1851
C		1383.81674(17)	1376	1388
$\mathbf{D_J}$	/kHz	0.5087(19)	0.571	0.581
$\mathbf{D_{JK}}$		1.102(12)	3.59	5.22
$\mathbf{D_K}$		[2.07][b]	2.07	0.247
$\mathbf{d_1}$		-0.1769(20)	-0.234	-0.230
$\mathbf{d_2}$		-0.0458(14)	-0.118	-0.151
χ_{aa}	/MHz	-1.1924(16)	-1.3607	-1.1187
χ_{bb}-χ_{cc}		-2.765(5)	-3.184	-2.596
$\mathbf{V_3}$	/kJ mol^{-1}	4.579(6)	2.6255[c]	4.50[c]
$\mathbf{F_0}$	/GHz	160.34(22)	157.43	157.44
δ	/rad	0.4829(7)	0.4213	0.4150
No. of lines		153		
$\boldsymbol{\sigma}^{\mathbf{d}}$	/kHz	2.4		

[a] Watson's S-reduced Hamiltonian (I^r representation). [b] Fixed to the calculated value. [c] Relative zero-point energy corrected. [d] Root-mean-square deviation of the fit.

Despite the sizeable dipole moments predicted for conformer II in Table 4.1, no transitions consistent with conformer II were observed. Additionally, even with the prior heating, the high boiling point of MCA resulted in signal intensities that were not sufficient to assign transitions due to minor isotopologues in natural abundance.

4.5. Discussion

The agreement of the experimentally derived spectroscopic constants for MCA in Table 4.2 with the quantum chemical estimates confirm that the observed rotational spectrum is of conformer I. The expected ground state structure, which is an expectation value over the LAM about ϕ, differs from the equilibrium geometry (corresponding to points Ia and Ib in Figure 4.1).

This is likely the origin of the discrepancies in some of the theoretical and experimental centrifugal distortion constants in Table 4.2, as the theoretical constants are based on harmonic estimates which would not account for this motion.

The heavy atom backbone of MCA lies largely in the *ab*-inertial plane, and thus the planar moment P_{cc} can provide some insight into the relationship between the ground state and equilibrium geometries. A study by Bohn *et al.*[13] of the contributions of CH_3 and CH_2 groups to P_{cc} for otherwise planar molecules showed that a relatively common value of 1.45-2.15 amu $Å^2$ is contributed for each methyl or methylene group in the molecule. For conformer II of MCA, using the predicted rotational constants given in Table 4.1, P_{cc} is 3.13 amu $Å^2$, and thus P_{cc}/n (where n is the number of CH_3 and CH_2 groups present in the molecule) is 1.57 amu $Å^2$. This is in the range reported for several formates (1.55-1.63 amu $Å^2$)[13], which is the closest structural equivalent to MCA reported in the data for that compilation. For conformer I of MCA, the P_{cc} value based on computational estimates is 3.66 amu $Å^2$, which suggests only minor contributions to the second moment when the cyano group is rotated out of the ester plane by ±10.1°. The experimental value of P_{cc}, however, is 4.36 amu $Å^2$, which suggests that the ground state heavy atom backbone is less planar as a result of these contributions. The flatness of the PES in ϕ about the global minima (Ia/Ib, Figure 4.3) helps to rationalize discrepancies in the literature as to the orientation of the cyano group in this conformer of MCA based on calculations using lower levels of theory and basis sets.[2,4,6–10] The near agreement of the theoretical and experimental rotational constants (Table 4.2) and larger than expected value of P_{cc} in this work suggest that the effective ground state geometry of conformer I of MCA is likely best characterized as having the cyano fragment oriented between the *gauche* and *anti* position relative to the carbonyl group but closer to the latter, which we term *near anti*.

The lack of observed transitions for conformer II indicates that this conformer is not metastable in the supersonic jet and thus undergoes relaxation to the lowest energy conformer. This process, termed conformational cooling, has been shown to occur when the barrier to interconversion is less than ~5 kJ mol^{-1} in an empirical study of many molecular systems.[14] The interconversion pathway for MCA shown in Figure 4.3 indicates an estimate of only 2.00 kJ mol^{-1} (B3LYP-D3(BJ)/aug-cc-pVTZ) for this barrier, which by the empirical guideline would suggest that the relaxation is facile. Additionally, as conformer I was the only conformer observed in the

rotational spectra, this unambiguously confirms that this is the lowest energy conformer of MCA, validating the theoretical results of the quantum chemical calculations performed here. This is in agreement with a prior B3LYP/6-31++G(d,p) calculation[10] and with a previous study of the gas-phase IR spectrum of MCA.[2] Further insight on the relative stability of conformer II is given in previous IR and Raman studies of MCA in condensed phases,[2–6] where it was shown that conformer II was the most abundant or the only form present depending on the sampling conditions. While not consistent with the results of the present study, it is noted that the *syn* conformer is more polar, with a dipole moment over double that of conformer I (7.74 D and 3.39 D, respectively), which suggests that the *syn* form becomes increasingly more stable when entering a condensed phase. This has been shown in matrix isolation studies of MCA, which examined conformational cooling effects as a function of deposition conditions.[8,9] As well, while conformer II was not detected in this study, since the publication of this first microwave spectrum, additional research was carried forth by Batra *et al*.[15] on MCA with a similar instrumental setup. Surprisingly, they were able to successfully identify conformer II and confirmed that this is the higher energy form. Using their reported rotational constants, we were able to locate a few very weak transitions in our original data, but our spectrum still supports that relaxation to conformer I which speaks to differences in the conditions of the supersonic jets in the two experiments.

The experimental barrier to internal rotation was derived using the XIAM program through a global fit of both A- and E-state transitions and found to be 4.579(6) kJ mol^{-1}, which is nearly twice as large as the ZPE-corrected estimate calculated at the B3LYP-D3(BJ)/aug-cc-pVTZ level of theory (2.63 kJ mol^{-1}) but is well estimated at the MP2/aug-cc-pVTZ level (4.50 kJ mol^{-1}). The experimental V_3 barrier for MCA is ~10% smaller than that of methyl acetate (V_3 = 5.0797(7) kJ mol^{-1} for the methyl ester).[16] Given that methyl rotors are highly sensitive to the electronic environment of the molecule,[17] this difference in the V_3 barrier suggests that the cyano fragment has a small influence on the electronic structure of MCA at the methyl substitution site. To study this effect further, NCI and NBO analyses were conducted.

The NCI isosurfaces (Figure 4.6), calculated for conformers I and II, map the attractive and repulsive intramolecular interactions at play. Both conformers have similar contacts between the hydrogens of the methyl group and the carbonyl oxygen due to the *syn* orientation of the methyl ester relative to the carbonyl, but an additional long-range contact is shown in the *near anti*

arrangement of the cyano fragment in conformer I between the cyano group and the oxygen of the ester. In Figure 4.6, this is seen in the NCI plot by the slight blue tinge on the isosurface between these two groups. This stabilizing effect is somewhat offset by a repulsive component (shown by the red tinge on the isosurface) which is associated by the formation of a 4-membered ring from the weak interaction. The balance between these two interactions is thus what governs the relative energies of conformers I and II.

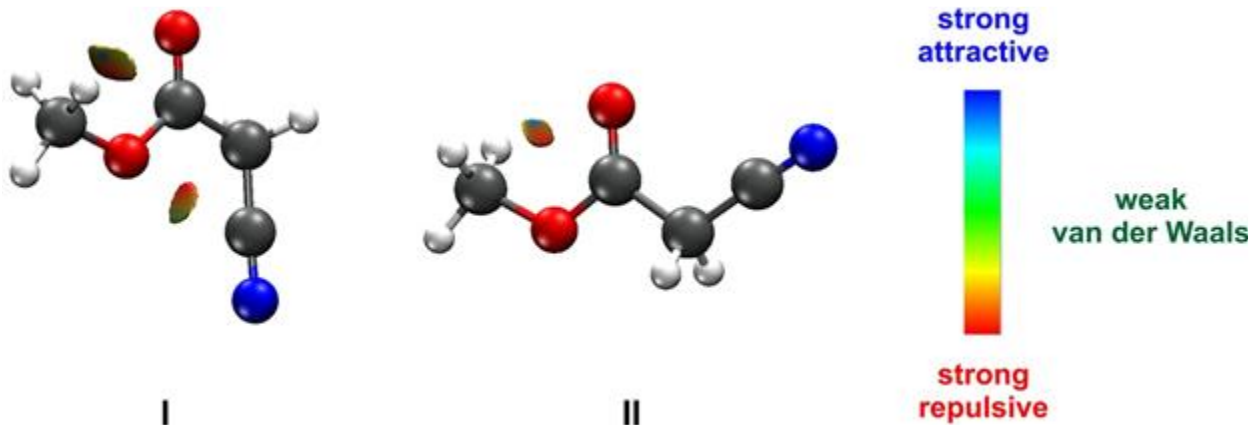

Figure 4.6. NCI isosurfaces (s = 0.05, colour scale of -0.02 < ρ < 0.02 au for the SCF densities) for the two most stable conformers of MCA.

To further quantify the effects governing the stability of the conformers of MCA, NBO calculations were conducted to decompose the full electronic energy of each conformer (ΔE_{total}) into its Lewis (ΔE_{Lewis}) and non-Lewis ($\Delta E_{non\text{-}Lewis}$) type contributions, which are summarized in Table 4.3. Here, steric and electrostatic effects are represented in the ΔE_{Lewis} portion, while the $\Delta E_{non\text{-}Lewis}$ portion represents stabilizing hyperconjugative orbital interactions. The NBO results summarized in Table 4.3 show large values of ΔE_{Lewis} for conformers III and IV (which both feature an *anti* arrangement of the methyl ester relative to the carbonyl), indicating a large destabilizing influence relative to conformers I and II. From inspection of the geometries of the conformers of MCA in Figure 4.2 and the nature of the occupied orbitals, the origin of this destabilization may be due to the antiparallel alignment of the C=O and C-O bonds as previous studies have suggested,[7,8] or possibly due to repulsion between the lone pairs on the ester and carbonyl oxygens.

Table 4.3. Relative energies of the Lewis (ΔE_{Lewis}, steric/electrostatic) and non-Lewis ($\Delta E_{non\text{-}Lewis}$, hyperconjugative) interactions, in kJ mol^{-1}, for the four conformers of MCA obtained from the NBO calculations at the B3LYP-D3(BJ)/aug-cc-pVTZ level of theory.

	ΔE_{Lewis}	$\Delta E_{non\text{-}Lewis}$
I	6.9	-8.5
II	0.0	0.0
III	31.7	-3.7
IV	35.0	-1.2

The results in Table 4.3 can also provide further insight into the relative energy ordering of conformers I and II. The larger value of ΔE_{Lewis} for conformer I indicates a larger destabilization due to steric effects than conformer II. However, this is accompanied by a greater stabilization due to hyperconjugative effects (reflected in the larger negative value for $\Delta E_{non\text{-}Lewis}$) when the cyano fragment is oriented *near anti* to the carbonyl. Comparing the second order perturbation corrections to the energies of conformers I and II from the NBO results, the nature of the stabilizing influences becomes clearer. For example, the orbital interaction characterized as LP(O-ester)→π*(C≡N) is only found in conformer I and was found to stabilize its geometry by 0.89 kJ mol^{-1}. Additionally, hyperconjugative effects involving the LP(O-ester)→π*(C=O) interaction are present in both conformers but were found to contribute an additional 2.16 kJ mol^{-1} to conformer I compared to conformer II. The donation of additional electron density from the lone pairs on the ester oxygen to other regions of the molecule is consistent with the decreased V_3 barrier found in this work for MCA when compared to that of methyl acetate.[16]

4.6. Conclusions

Using microwave spectroscopy with high-level quantum chemical calculations, the global minimum geometry of MCA, labelled conformer I here, was conclusively shown to have the methyl and cyano fragments oriented *syn* and *near anti*, respectively, to the carbonyl group. This determination settles a decades-long discrepancy in the literature, which indicated that the lowest energy conformer of MCA had a *syn*/*syn* orientation of these fragments, termed conformer II here, consistent with earlier theoretical studies.[2,4,6–9] The ground state geometry is highly averaged over a large-amplitude motion involving the cyano fragment moving out of the plane of the heavy atom

backbone of the molecule. This averaging, resulting in a relative flatness of the PES associated with the C-C-C=O dihedral angle, likely contributed to the challenges in establishing the global minimum geometry of MCA. Through NBO calculations, it was found that increased hyperconjugative interactions such as LP(O-ester)→π*(C≡N) and LP(O-ester)→π*(C=O) are responsible for the slight balance in favour for conformer I over conformer II, calculated to be 1.4 kJ mol^{-1} (B3LYP-D3(BJ)/aug-cc-pVTZ). The experimentally derived spectroscopic constants and parameters associated with the methyl rotor serve as groundwork to investigate MCA in the millimetrewave region and may lead to its detection in astronomical sources.

4.7. References

(1) Tercero, B.; Kleiner, I.; Cernicharo, J.; Nguyen, H. V. L.; López, A.; Caro, G. M. M. Discovery of Methyl Acetate and Gauche Ethyl Formate in Orion. *Astrophys. J. Lett.* **2013**, *770* (1), L13.

(2) Leibowitz, S.; Laane, J.; van Alsenoy, C.; der Veken, B. J. Van. On the Conformational Analysis of Methyl Cyanoacetate. *J. Mol. Struct.* **1991**, *248*, 251–273.

(3) Charles, S. W.; Jones, G. I. L.; Owen, N. L. Vibrational Spectra and Rotational Isomerism of Methyl and Ethyl Cyanoacetate. *J. Chem. Soc.{,} Faraday Trans. 2* **1973**, *69* (0), 1454–1464.

(4) Prasad, R.; Mishra, Y.; Gupta, R. Spectroscopic and Molecular Mechanics Study of the Conformational Properties of Methyl Cyanoacetate and Ethyl Cyanoacetate. *Indian J. Chem. -Section A* **1990**, *29* (07), 618–623.

(5) Sinha, D.; Katon, J. E. The Vibrational Spectra of Methyl Cyanoacetate and Methyl Cyanoacetate- d 3 . *Can. J. Chem.* **1974**, *52* (17), 3057–3062.

(6) Maury, C.; Petrissans, J. Analyse Structurale Des Dérivés Fonctionnels Des Acides Carboxyliques Partie II. Halogèno et Cyanoacétates de Méthyle. *J. Mol. Struct.* **1991**, *246* (3), 267–278.

(7) Neta, J. M. F.; Fausto, R. Molecular Structure and Vibrational Spectra of Methyl Cyanoacetate: An FT-IR, Raman and Ab Initio Molecular Orbital Study. *J. Mol. Struct.* **1998**, *443* (1), 41–56.

(8) Reva, I. D.; Ilieva, S. V.; Fausto, R. Conformational Isomerism in Methyl Cyanoacetate: A Combined Matrix-Isolation Infrared Spectroscopy and Molecular Orbital Study. *Phys. Chem. Chem. Phys.* **2001**, *3* (19), 4235–4241.

(9) Reva, I. D.; Stepanian, S. G.; Adamowicz, L.; Fausto, R. Missing Conformers. Comparative Study of Conformational Cooling in Cyanoacetic Acid and Methyl Cyanoacetate Isolated in Low Temperature Inert Gas Matrixes. *Chem. Phys. Lett.* **2003**, *374* (5), 631–638.

(10) Popova, A. D.; Binev, Y. I.; Vassileva-Boyadjieva, P. J.; Binev, I. G. Experimental IR, and Computational Ab Initio and DFT B3LYP Studies on Spectral and Structural Changes, Caused by the Conversion of Methyl Cyanoacetate into Carbanion. *Bulg. Chem. Commun.* **2008**, *40* (4), 512–519.

(11) Western, C. M. PGOPHER: A Program for Simulating Rotational, Vibrational and Electronic Spectra. *J. Quant. Spectrosc. Radiat. Transf.* **2017**, *186*, 221–242.

(12) Hartwig, H.; Dreizler, H. The Microwave Spectrum of Trans-2,3-Dimethyloxirane in Torsional Excited States. *Zeitschrift für Naturforsch. A* **1996**, *51* (8), 923–932.

(13) Bohn, R. K.; Montgomery, J. A.; Michels, H. H.; Fournier, J. A. Second Moments and Rotational Spectroscopy. *J. Mol. Spectrosc.* **2016**, *325*, 42–49.

(14) Ruoff, R. S.; Klots, T. D.; Emilsson, T.; Gutowsky, H. S. Relaxation of Conformers and Isomers in Seeded Supersonic Jets of Inert Gases. *J. Chem. Phys.* **1990**, *93* (5), 3142–3150.

(15) Batra, G.; Schnell, M.; Steber, A.; Pinacho, P. Comprehensive Rotational Spectroscopy of Methyl Cyanoacetate for Astronomical Searches. In *Proceedings of the 2021 International Symposium on Molecular Spectroscopy*; University of Illinois at Urbana-Champaign: Urbana, Illinois, 2021; pp 1–1.

(16) Nguyen, H. V. L.; Kleiner, I.; Shipman, S. T.; Mae, Y.; Hirose, K.; Hatanaka, S.; Kobayashi, K. Extension of the Measurement, Assignment, and Fit of the Rotational Spectrum of the Two-Top Molecule Methyl Acetate. *J. Mol. Spectrosc.* **2014**, *299*, 17–21.

(17) Spangler, L. H. Structural Information from Methyl Internal Rotation Spectroscopy. *Annu. Rev. Phys. Chem.* **1997**, *48* (1), 481–510.

Chapter 5 – 2-methyl- and 2-ethyl-2-oxazoline

5.1. Introduction

Methyl-substituted 2-oxazoline derivatives such as 2-methyl-2-oxazoline (2M2O) and 2-ethyl-2-oxazoline (2E2O) are primarily used in the formation of polymers, as they can readily undergo a ring-opening reaction that allows for the production of well-defined polymers, the composition of which is readily tunable by the use of varying initiating and terminating reagents.[1–4] These polymers have promising applications in forming biomaterials and as green alternatives to oil-based polymers.[1] Along with these applications, the molecules exhibit complex internal dynamics that arise from their electronic properties. Thus, their study on a fundamental level allows for an exploration of these dynamics.

Their parent compound, 2-oxazoline, has been studied using microwave, millimetre-wave, infrared, and Raman spectroscopy,[5,6] with most of its attention focused on the conformation of the heavy atom backbone of the ring. While initially thought to be planar, it was found that the ring was puckered with a barrier to planarity of only 49(8) J mol^{-1}.[6] Furthermore, this planarity was found to be poorly captured by most quantum chemical methods, with only calculations done using the MP2 method yielding a puckered structure.[6]

The electronic environment of a methyl rotor has been known to play a role in the size and shape of its barrier to internal rotation.[7] Previous studies on methyl-substituted aromatic heterocyclic molecules have found significant differences in these barriers based on the position of the methyl substituent in the ring,[8–10] and also based on the conformations of other groups on the ring.[11] While there have been many studies looking at these systems on aromatic heterocyclic molecules, very little has been done for methyl rotors on partially saturated heterocyclic rings.

In this study, rotational spectroscopy was used to probe the internal dynamics of 2M2O and 2E2O for the first time, revealing complicated spectra that featured torsional splittings due to the hindered rotation of the methyl group and hyperfine structure due to the presence of a ^{14}N nucleus. Analysis of these splittings led to the determination of the V_3 barriers for 2M2O and one conformer of 2E2O, aided by high-level quantum chemical calculations. The barrier heights were compared with previous studies of other methylated five-membered heterocycles in order to draw insight into the factors that influence their V_3 barriers.

5.2. Computational Methods

As a first step, *ab initio* calculations were carried out to determine predicted geometries, rotational constants, conformational preferences and parameters related to the methyl internal rotors. Both 2M2O and 2E2O contain a partially unsaturated 5-membered ring, and so the heavy atom backbone of the ring can either take on a planar configuration or a puckered configuration.[12] Additionally, for 2E2O, the ethyl side chain can also rotate, leading to further possibilities for conformational arrangements. Potential energy surface (PES) scans were conducted to determine the conformation of the ring for both molecules and the conformational preference of the ethyl side chain for 2E2O. The PES for 2E2O, shown in Figure 5.1, showed that the ethyl fragment can lie *syn* to the double bond in the ring or tilted ±115° in a *gauche* conformation, leading to a mirror image pair.

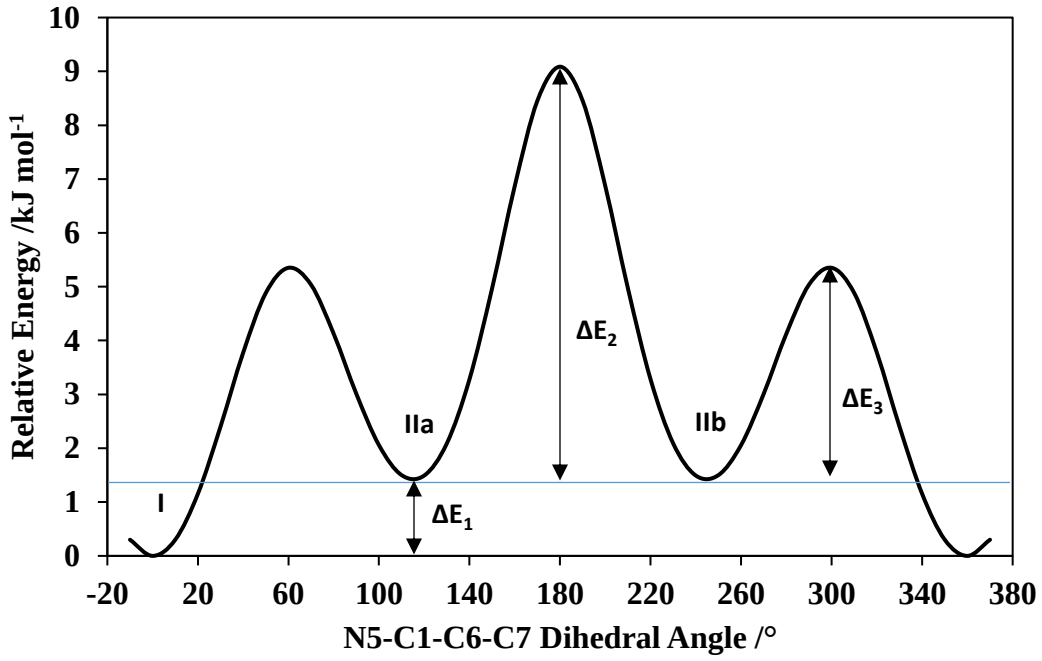

Figure 5.1. Conformational landscape for 2E2O calculated by stepping the dihedral angle of the ethyl fragment relative to the double bond in the ring at the B3LYP-D3(BJ)/aug-cc-pVTZ level of theory. The energy difference that separates conformers I and II (ΔE_1) is 1.49 kJ mol^{-1}, while the energy barriers for the interconversion between the mirror images for conformer II (ΔE_2) and the interconversion between conformers I and II (ΔE_3) are 7.59 kJ mol^{-1} and 3.86 kJ mol^{-1}, respectively.

The geometries (given in Figure 5.2) were then optimized and verified to be true minima using frequency analyses. Since the parent molecule, 2-oxazoline,[6] displayed a strong dependency of the geometry on the level of theory, calculations were done using both DFT methods (B3LYP-D3(BJ)/aug-cc-pVTZ) and *ab initio* methods (MP2/aug-cc-pVTZ) which are summarized in Table 5.1.

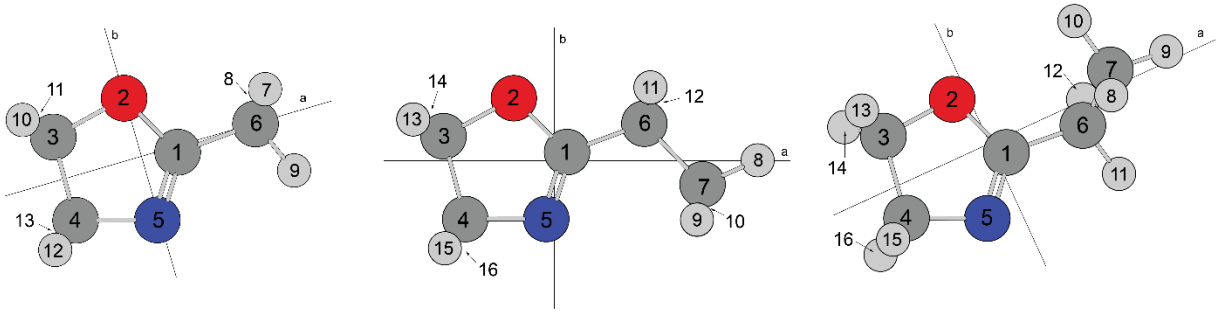

Figure 5.2. Equilibrium structures for 2M2O (left), 2E2O-I (center) and 2E2O-II (right) calculated at the B3LYP-D3(BJ)/aug-cc-pVTZ level of theory. Note that 2E2O-II exists as a mirror image pair, with the terminal methyl tilted ±115° out of the plane.

Table 5.1. Calculated parameters for 2M2O and both conformers of 2E2O, calculated at the B3LYP-D3(BJ)/aug-cc-pVTZ (labeled DFT here) and MP2/aug-cc-pVTZ levels of theory.

		2M2O		**2E2O-I**		**2E2O-II**	
		DFT	**MP2**	**DFT**	**MP2**	**DFT**	**MP2**
A	/MHz	7799.6	7778.0	6503.3	6467.3	6098.5	6047.6
B		3425.3	3444.5	1885.9	1908.9	1906.4	1937.0
C		2490.5	2507.6	1516.6	1533.4	1620.1	1643.0
μ_a	/Debye	0.71	0.79	0.94	1.04	0.47	0.53
μ_b		1.10	1.10	0.74	0.69	1.25	1.28
μ_c		0.00	0.03	0.00	0.05	0.06	0.09
V_3 [a]	/kJ mol^{-1}	4.29	4.62	9.39	10.39	10.78	11.59
Energy [a]				0	0	1.93	1.58
Population [b]				68.5%	65.4%	31.5%	34.6%

[a] Relative zero-point energy corrected. [b] Boltzmann population at 298 K.

Finally, since both molecules contain a methyl rotor, additional PES scans were calculated to estimate the barriers to internal rotation (shown below in Figure 5.3), which enabled a prediction of the degree of peak splitting possible due to the methyl rotor. All calculations were carried out using Gaussian Rev. C.01.[13]

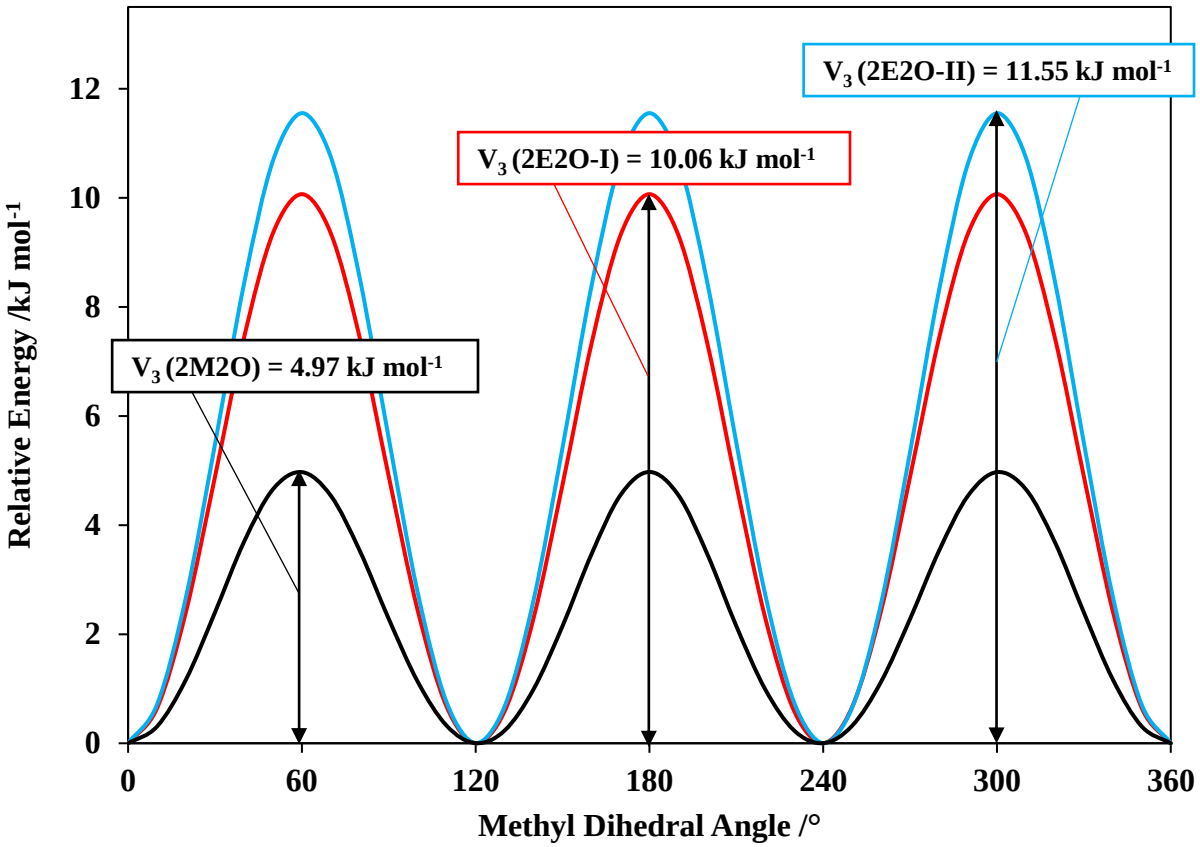

Figure 5.3. Internal rotation potential energy scan for 2M2O (black), 2E2O-I (red) and 2E2O-II (blue) calculated at the B3LYP-D3(BJ)/aug-cc-pVTZ level of theory.

5.3. Experimental

Commercial samples of 2M2O (Alfa Aesar, 99%) and 2E2O (Sigma-Aldrich, ≥99%) were purchased and used without further purification. The rotational spectra of both molecules were collected using chirped-pulse (cp) and Balle-Flygare (bf) Fourier-transform microwave (FTMW) spectrometers, the details of which have been previously described.[14,15] The samples were placed in glass bubblers and seeded into a neon carrier gas to be delivered to the instrument. The broadband spectra were first collected using the cp-FTMW from 7 – 19 GHz to make preliminary

assignments, after which the assigned lines were recollected with the higher resolution bf-FTMW spectrometer to resolve splittings due to the nuclear hyperfine structure due to ^{14}N and A/E splittings due to the internal rotors.

5.4. Spectral Analysis

The calculations for 2M2O revealed dipole moments along the *a*- and *b*-inertial axes of 0.71 D and 1.10 D, respectively (B3LYP-D3(BJ)/aug-cc-pVTZ), indicating that the spectrum should present with strong *a*- and *b*-type transitions. The spectrum was simulated in PGOPHER[16] using the calculated rotational constants (Table 5.1), from which the transitions of 2M2O were assigned. As with 2-oxazoline, the spectrum of 2M2O was dominated by Q-branch transitions.[6]

The complex splitting patterns due to the internal rotor and the ^{14}N quadrupole nucleus were resolved by measurements taken with the bf-FTMW spectrometer. The resulting 212 lines were fit using the XIAM program[17] to determine the rotational spectroscopic parameters and the parameters relating to the internal rotor with a rms deviation of 2.6 kHz. Unlike with MCA, the addition of the higher order terms Dpi_{2J} and Dpi_{2K} were required to obtain a fit with an error within experimental accuracy, which account for the coupling between the internal rotation and the overall rotation of the molecule.[18] In addition, the minor ^{13}C and ^{15}N isotopologues were assigned and fit following a similar procedure as the parent species. These experimentally determined constants for both the parent species and the minor isotopologues are summarized in Table 5.2.

Table 5.2. Spectroscopic constants and internal rotation parameters derived for 2M2O and its observed minor isotopologues.[a,b] See Figure 5.2 for atomic numbering for 2M2O.

		Parent	**^{13}C1**	**^{13}C3**	**^{13}C4**	**^{15}N5**	**^{13}C6**
A	/MHz	7747.7085(5)	7746.84796(29)	7679.5268(3)	7680.81047(27)	7589.1844(7)	7747.73085(26)
B		3425.67485(18)	3415.58179(29)	3381.1500(4)	3378.9691(3)	3425.7399(6)	3322.17858(19)
C		2489.91616(16)	2484.49560(27)	2459.4257(3)	2458.37018(26)	2473.3482(7)	2434.77304(19)
Δ_J	/kHz	0.239(5)	0.215(12)	0.203(15)	0.204(13)	0.202(28)	0.208(10)
Δ_{JK}		1.13(4)	[1.13]	[1.13]	[1.13]	[1.13]	[1.13]
Δ_K		1.08(9)	[1.08]	[1.08]	[1.08]	[1.08]	[1.08]
δ_J		0.0613(19)	0.059(3)	0.063(4)	0.064(3)	0.061(7)	[0.0613]
δ_K		0.36(4)	[0.36]	[0.36]	[0.36]	[0.36]	[0.36]
χ_{aa}	/MHz	2.0103(9)	2.0184(17)	1.9846(15)	2.0393(21)		2.0093(21)
χ_{bb}- χ_{cc}		-4.5261(17)	-4.510(4)	-4.491(4)	-4.544(4)		-4.523(4)
V_3	/kJ mol^{-1}	5.3779(4)	5.37964(28)	5.3756(4)	5.37522(28)	5.3836(21)	5.3810(7)
F_0	/GHz	[159.6]	[159.6]	[159.6]	[159.6]	[159.6]	[159.6]
F[c]		167.8	167.8	167.7	167.7	167.6	167.8
δ	/rad	3.119(11)	3.112(6)	3.083(4)	3.108(5)	3.112(28)	3.120(11)
Dpi_{2J}	/GHz	3.1(6)x10^{-5}	[3.1x10^{-5}]	[3.1x10^{-5}]	[3.1x10^{-5}]	[3.1x10^{-5}]	[3.1x10^{-5}]
Dpi_{2K}		-7.15(27)x10^{-4}	[-7.15x10^{-4}]	[-7.15x10^{-4}]	[-7.15x10^{-4}]	[-7.15x10^{-4}]	[-7.15x10^{-4}]
N		212	59	69	59	20	44
σ[d]	/kHz	2.6	2.2	2.4	2.5	2.3	2.3

[a] Watson's A-reduced Hamiltonian (I^r representation). [b] Values in square brackets fixed to calculated values. [c] Derived. [d] Root-mean-square deviation of the fit.

The conformational landscape of 2E2O varied slightly compared with 2M2O, as there are two possible conformations the molecule can take, however, the procedure followed that of 2M2O. For both conformers of 2E2O, the spectrum was dominated by strong *a*- and *b*-type transitions. From the predicted spectra, the strongest lines were readily assigned to 2E2O-I, and by scaling the experimentally determined constants, the ^{13}C and ^{15}N minor isotopologues were identified as well. Once these lines had been removed from the spectrum, the remaining strong lines were assigned to conformer II. Unlike conformer I, the intensities of these transitions were insufficient as to be able to assign minor isotopologues. As with 2M2O, the hyperfine splittings for both conformers were resolved using the bf-FTMW spectrometer. The splittings due to the internal rotation, however, were only partially resolved for 2E2O-I for certain transitions as the predicted barrier is nearly double that of 2M2O. The differences in the splitting patterns for 2M2O and 2E2O-I are given below in Figure 5.4. For 2E2O-II, which had an even larger predicted barrier, no splittings were resolved. Both conformers were fit with XIAM,[17] the results of which are given in Table 5.3 and Table 5.4.

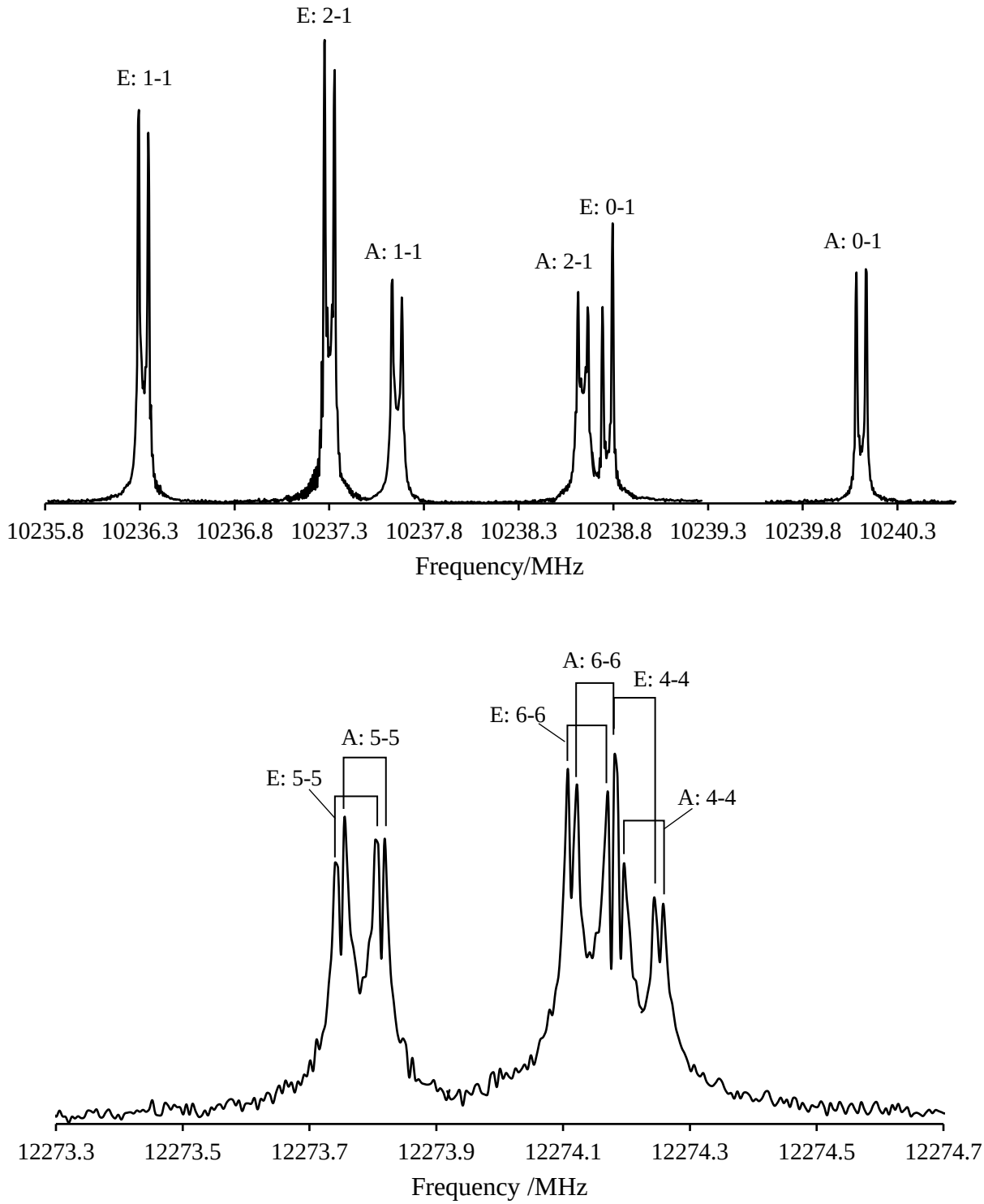

Figure 5.4. (above) The 111-000 transition for 2M2O, detailing the large separations between A- and E-state hyperfine components. (below) The 523-514 transition for 2E2O-I.

Table 5.3. Experimentally determined spectroscopic parameters for 2E2O-I and its observed minor isotopologues.[a,b] See Figure 5.2 for atomic numbering for 2E2O-I.

		Parent	**^{13}C1**	**^{13}C3**	**^{13}C4**	**^{15}N5**	**^{13}C6**	**^{13}C7**
A	/MHz	6447.78918(17)	6445.8741(5)	6432.0597(5)	6360.61396(25)	6358.7314(8)	6410.906(5)	6433.3942(7)
B		1892.0575(5)	1891.83695(11)	1864.14953(16)	1873.74493(18)	1891.95551(20)	1873.75904(15)	1843.20450(12)
C		1520.5039(5)	1520.25633(11)	1501.61158(12)	1503.83944(15)	1515.43441(20)	1506.64395(15)	1488.02805(12)
Δ_J	/kHz	0.1382(11)	0.1363(10)	0.1334(15)	0.1484(15)	0.1376(18)	0.1397(14)	0.1389(10)
Δ_{JK}		[-0.01005]	[-0.01005]	[-0.01005]	[-0.01005]	[-0.01005]	[-0.01005]	[-0.01005]
Δ_K		[1.498]	[1.498]	[1.498]	[1.498]	[1.498]	[1.498]	[1.498]
δ_J		0.0313(9)	0.0263(13)	0.0324(15)	0.0325(20)	0.0274(24)	0.0256(17)	0.0333(14)
δ_K		[0.1671]	[0.1671]	[0.1671]	[0.1671]	[0.1671]	[0.1671]	[0.1671]
χ_{aa}	/MHz	1.0871(10)	1.0805(12)	1.091(3)	1.122(6)		1.109(3)	1.047(3)
χ_{bb}- χ_{cc}		-3.6021(20)	-3.628(5)	-3.580(5)	-3.663(7)		-3.602(12)	-3.543(12)
F_0	/GHz	[161.1]	[161.1]	[161.1]	[161.1]	[161.1]	[161.1]	[161.1]
F^c		165.6	165.6	165.6	165.6	165.6	165.6	165.6
V_3	/kJ mol^{-1}	10.88(6)	[10.88]	[10.88]	[10.88]	[10.88]	[10.88]	[10.88]
δ	/rad	2.40(3)	[2.40]	[2.40]	[2.40]	[2.40]	[2.40]	[2.40]
N		284	33	36	33	12	32	28
σ^d	/kHz	2.8	1.8	2.8	2.7	1.4	2.2	1.8

[a] Watson's A-reduced Hamiltonian (I^r representation). [b] Values in square brackets fixed to calculated values. [c] Derived. [d] Root-mean-square deviation of the fit.

Table 5.4. Experimentally observed spectroscopic constants for 2E2O-II.[a,b]

		XIAM
A	/MHz	6060.0318(3)
B		1914.10980(20)
C		1622.97356(14)
Δ_J	/kHz	0.3004(20)
Δ_{JK}		2.357(8)
Δ_K		[1.410]
δ_J		0.0128(17)
δ_K		[1.109]
χ_{aa}	/MHz	2.1642(16)
χ_{bb}- χ_{cc}		-4.687(3)
N		102
σ^c	/kHz	3.7

[a] Watson's A-reduced Hamiltonian (I^r representation). [b] Values in square brackets fixed to calculated values. [c] Root-mean-square deviation of the fit.

5.5. Discussion

The observation of ^{13}C and ^{15}N minor isotopologues for 2M2O and 2E2O-I allowed for the derivation of their Kraitchman[19] substitution (r_s) structures. These were determined using Kisiel's KRA program,[20] with the relative signs of the coordinates obtained by comparison to the calculated coordinates (B3LYP-D3(BJ)/aug-cc-pVTZ). The Kraitchman coordinates along with their Costain errors[21] were used with the EVAL program[20] to derive the internal parameters relating to the carbon and nitrogen sites. These parameters are given for both molecules in Table 5.5 and Table 5.6, along with their calculated values. The numbering schemes for both molecules is given above in Figure 5.2.

Table 5.5. Experimentally determined substitution (r_s) structure for 2M2O.

		r_s	B3LYP-D3(BJ) /aug-cc-pVTZ	MP2 /aug-cc-pVTZ
C3-C4	/Å	1.540(4)	1.546	1.535
C4-N5		1.487(28)	1.469	1.473
N5-C1		1.276(21)	1.266	1.277
C1-C6		1.491(4)	1.485	1.484
C3-C4-N5	/°	104.6(6)	104.7	104.5
C4-N5-C1		105.2(10)	107.1	105.9
N5-C1-C6		123(3)	127	127
C6-C1-N5-C4		-179(9)	180	176
C1-N5-C4-C3		5(15)	0	10

Table 5.6. Experimentally determined r_s structure for 2E2O-I.

		r_s	B3LYP-D3(BJ) /aug-cc-pVTZ	MP2 /aug-cc-pVTZ
C3-C4	/Å	1.538(5)	1.546	1.535
C4-N5		1.497(13)	1.469	1.473
N5-C1		1.242(10)	1.266	1.277
C1-C6		1.534(9)	1.491	1.488
C6-C7		1.525(4)	1.523	1.520
C3-C4-N5	/°	104.88(26)	104.7	104.4
C4-N5-C1		103.5(7)	107.2	105.9
N5-C1-C6		123.8(9)	127.3	126.9
C1-C6-C7		113.5(4)	113.7	112.8
C6-C1-N5-C4		-179(5)	180	177
C1-N5-C4-C3		4(6)	0	11

As with 2-oxazoline,[6] the estimated geometries for the ring structure in 2M2O and 2E2O-I were sensitive to the computational method chosen, with B3LYP predicting a planar heavy atom

backbone and MP2 predicting a puckered structure. A scan of the C1-N5-C4-C3 dihedral angle for 2M2O at the MP2/aug-cc-pVTZ level of theory shows a symmetric double well potential with equivalent minima at ±11° (Figure 5.5), whose transition state at 0º has a predicted geometry wherein all other dihedral angles are at 0° as well. The transition state structure was reoptimized at the same level of theory. Through frequency analyses, the barrier to planarity was determined to be below the zero-point energy for either of the minima. The ground state and transition state structures for 2E2O-I were optimized with frequency analyses using the same level of theory, which also showed that the transition state lay below the zero-point energy for the minima. The experimentally derived C1-N5-C4-C3 dihedral angles for 2M2O (Table 5.5) and 2E2O-I (Table 5.6) lie partially between the DFT and MP2 values. However, as the intensities of the ^{18}O isotopologues for both molecules were not intense enough to be fitted, the r_s structures cannot tell whether the oxygen lies in the same plane as the other atoms in the ring or not. As is evident, the errors associated with these geometric parameters are significant, due to the significant Costain errors obtained from the Kraitchmann coordinates, which are known to occur in molecules with untreated vibrational effects consistent with low-lying LAMs.[22] Attempts to determine a semi-experimental structure using the STRFIT program[20] resulted in substantial rms values, likely due to the ground state structure lying somewhere between the DFT (planar ring backbone) and MP2 (puckered ring) equilibrium structures. This unaccounted-for motion of the ring structures would also contribute to the discrepancies between the calculated and experimental centrifugal distortion constants, as the calculated values are derived from the harmonic frequencies, which would not correctly account for the out-of-plane puckering of the ring represented by the potentials derived here. This was similarly observed in methyl cyanoacetate, as described in this thesis' previous chapter.

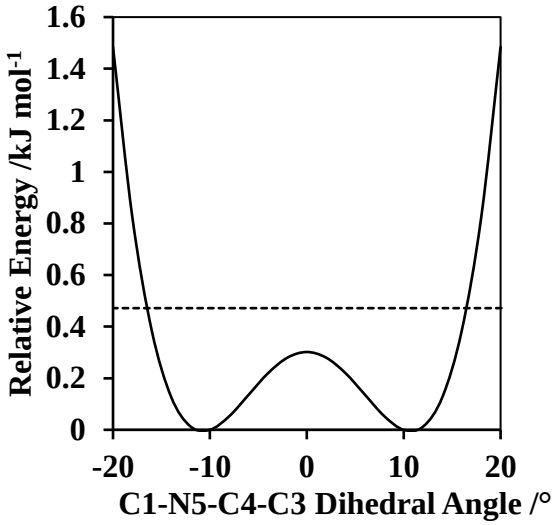

Figure 5.5. Potential energy curve for the ring puckering of 2M2O calculated at the MP2/aug-cc-pVTZ level of theory. The dashed line represents the zero-point energy of the two equivalent minima.

The experimentally derived V_3 barriers for 2M2O and 2E2O-I were 5.3779(4) kJ mol^{-1} and 10.88(6) kJ mol^{-1}, respectively. When comparing these values with the zero-point energy-corrected barrier heights obtained from calculations (Table 5.1), the barrier for 2M2O was underestimated by 20% by the B3LYP method and by 14% using MP2, whereas for 2E2O-I these underestimates were smaller, with B3LYP predicting a barrier 14% smaller and MP2 predicting one at just 5% smaller. This follows what was observed with MCA, wherein the barrier height predicted using MP2 was much more closely aligned with experimental values than the barrier predicted by B3LYP. The observation that the barrier height was more poorly predicted for 2M2O than 2E2O-I is indicative of a trend seen in other compounds containing methyl rotors, where lower torsional barriers are poorly predicted by calculations.[23] By extrapolation of the discrepancies seen between the calculated and experimental V_3 barriers for 2E2O-I, we can estimate that the true barrier for 2E2O-II is likely above 12 kJ mol^{-1}, for which the predicted A- and E-state transitions are entirely superimposed. This supposition is further supported by the lack of resolvable splitting seen in the experimental spectra for 2E2O-II.

The sensitivity of the V_3 barrier to electronic structure becomes apparent when comparing barrier heights for methyl substituents on other small heterocycles, as shown in Figure 5.6. Aromatic heterocycles had consistently lower barrier heights than the partially unsaturated

heterocycles studied in this work. In particular, the barrier height for 2M2O (5.38 kJ mol^{-1}) is nearly double that of 2-methyloxazole (3.01 kJ mol^{-1}),[8] and the barrier height for 2E2O-I (10.88 kJ mol^{-1}) is over three times as large. From hyperconjugative models based on small aliphatic molecules with a single double bond such as propene, aldehydes, and ketones, the interactions of the π_{CH_3} orbitals with the π orbitals of the double bond have a destabilizing effect that contributes to the V_3 potential.[24] As such, a possible explanation of the smaller barriers in aromatic compounds is that this destabilization effect is minimized when compared to the partially unsaturated systems in 2M2O and 2E2O.

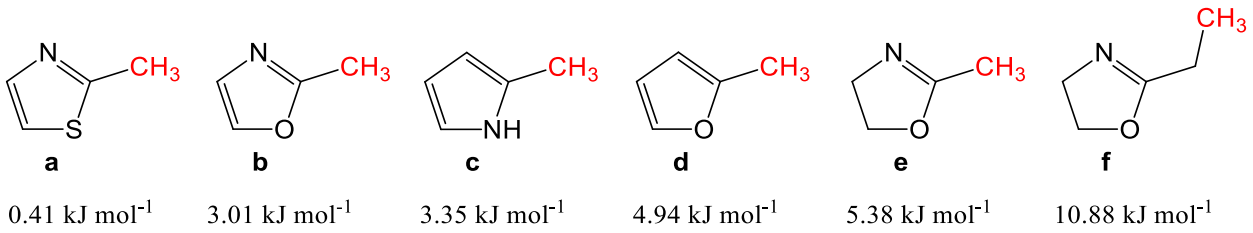

Figure 5.6. Comparison of V_3 barriers in (a) 2-methylthiazole,[25] (b) 2-methyloxazole,[8] (c) 2-methylpyrrole,[9] (d) 2-methylfuran,[11] (e) 2M2O (this work), and (f) 2E2O-I (this work).

Additionally, the electronic properties of the two neighbouring ring sites of the methyl-substituted carbon site have a notable effect. For the methylated oxazoles, the V_3 barrier when the methyl is between the two heteroatoms (3.01 kJ mol^{-1}) is much lower than when it is in the 4- (5.14 kJ mol^{-1}) or 5- (5.72 kJ mol^{-1}) positions on the ring.[8] A similar effect was demonstrated with 2- and 3-methylpyrrole, where 2-methylpyrrole had a slightly higher barrier (3.35 kJ mol^{-1})[9] than 3-methylpyrrole (2.94 kJ mol^{-1}).[10] In aromatic ring systems, this discrepancy is thought to be a result of the two adjacent sites to the methyl substitution site contributing a V_3 potential to the barrier opposite in phase.[24] Namely, if the electronic density on the directly adjacent sites to the methyl substitution site are of a similar magnitude, the V_3 contributions have a cancellation effect that results in a lower barrier.[24] It is unclear whether this principle holds in the case of a non-aromatic ring system as in 2M2O or in the case of the methyl rotor being one site removed from the ring as in 2E2O-I, but it is a possible contributing factor to the much larger barrier seen in 2E2O-I.

5.6. Conclusions

The microwave spectra of 2M2O and both conformers of 2E2O were analyzed for the first time using FTMW spectroscopy in conjunction with high-level quantum chemical calculations,

allowing for the determination of their rotational constants, centrifugal distortion constants, nuclear quadrupole coupling constants and parameters related to the hindered internal rotor of the terminal methyl groups. While the singly substituted ^{13}C and ^{15}N minor isotopologues were also recorded for 2M2O and 2E2O-I, the likely presence of a low-lying ring puckering motion resulted in large uncertainties for key geometric parameters. The V_3 barriers obtained in this work were contrasted with other five-membered heterocyclic molecules, which were found to vary based on the aromaticity and the position of the heteroatoms in the ring. Further study into methyl substituted, partially unsaturated heterocycles are warranted to examine these effects in greater detail.

5.7. References

(1) Hoogenboom, R. Poly(2-Oxazoline)s: Alive and Kicking. *Macromol. Chem. Phys.* **2007**, *208* (1), 18–25.

(2) Hoogenboom, R. Poly(2-Oxazoline)s: A Polymer Class with Numerous Potential Applications. *Angew. Chemie Int. Ed.* **2009**, *48* (43), 7978–7994.

(3) Schlaad, H.; Diehl, C.; Gress, A.; Meyer, M.; Levent Demirel, A.; Nur, Y.; Bertin, A. Poly(2-Oxazoline)s as Smart Bioinspired Polymers. *Macromol. Rapid Commun.* **2010**, *31* (6), 511–525.

(4) Hu, F.; Xie, S.; Jiang, L.; Shen, Z. Living Cationic Ring-Opening Polymerization of 2-Oxazolines Initiated by Rare-Earth Metal Triflates. *RSC Adv.* **2014**, *4* (104), 59917–59926.

(5) Durig, J. R.; Riethmiller, S.; Li, Y. S. Spectra and Structure of Small Ring Compounds. XXXI Microwave, Raman and Infrared Spectra, Conformation, Dipole Moment, and Quadrupole Coupling Constants of 2-oxazoline. *J. Chem. Phys.* **1974**, *61* (1), 253–262.

(6) Samdal, S.; Møllendal, H.; Reine, S.; Guillemin, J. C. Ring Planarity Problem of 2-Oxazoline Revisited Using Microwave Spectroscopy and Quantum Chemical Calculations. *J. Phys. Chem. A* **2015**, *119* (20), 4875–4884.

(7) Shirar, A. J.; Wilcox, D. S.; Hotopp, K. M.; Storck, G. L.; Kleiner, I.; Dian, B. C. Impact of Molecular Conformation on Barriers to Internal Methyl Rotation: The Rotational Spectrum of m-Methylbenzaldehyde. *J. Phys. Chem. A* **2010**, *114* (46), 12187–12194.

(8) Fliege, E. R. L. A Reanalysis of 14 N Nuclear Quadrupole Coupling and Methyl Internal Rotation in the Rotational Spectra of Monomethyl Oxazoles and Isoxazoles. *Zeitschrift für Naturforsch. A* **1990**, *45* (7), 911–922.

(9) Nguyen, T.; Dindic, C.; Stahl, W.; Nguyen, H. V. L.; Kleiner, I. 14N Nuclear Quadrupole Coupling and Methyl Internal Rotation in the Microwave Spectrum of 2-Methylpyrrole. *Mol. Phys.* **2020**, *118* (11), 1668572.

(10) Nguyen, T.; Stahl, W.; Nguyen, H. V. L.; Kleiner, I. 14N Nuclear Quadrupole Coupling and Methyl Internal Rotation in 3-Methylpyrrole Investigated by Microwave Spectroscopy. *J. Mol. Spectrosc.* **2020**, *372*.

(11) Hakiri, R.; Derbel, N.; Vinh Lam Nguyen, H.; Mouhib, H. Communication through the Furan Ring: The Conformational Effect on the Internal Rotation of 5-Methyl Furfural Studied by Microwave Spectroscopy Communication through the Furan Ring: Conformational Effect on the Internal Rotation of 5-Methyl Furfural Studied by Microwave Spectroscopy. *Phys. Chem. Chem. Phys.* **2018**, *20* (40), 1–8.

(12) Legon, A. C. Equilibrium Conformations of Four- and Five-Membered Cyclic Molecules in the Gas Phase: Determination and Classification. *Chem. Rev.* **1980**, *80* (3), 231–262.

(13) Frisch, M. J.; Trucks, G. W.; Schlegel, H. B.; Scuseria, G. E.; Robb, M. a.; Cheeseman, J. R.; Scalmani, G.; Barone, V.; Petersson, G. a.; Nakatsuji, H.; Li, X.; Caricato, M.; Marenich, a. V.; Bloino, J.; Janesko, B. G.; Gomperts, R.; Mennucci, B.; Hratchian, H. P.; Ortiz, J. V.; Izmaylov, a. F.; Sonnenberg, J. L.; Williams; Ding, F.; Lipparini, F.; Egidi, F.; Goings, J.; Peng, B.; Petrone, A.; Henderson, T.; Ranasinghe, D.; Zakrzewski, V. G.; Gao, J.; Rega, N.; Zheng, G.; Liang, W.; Hada, M.; Ehara, M.; Toyota, K.; Fukuda, R.; Hasegawa, J.; Ishida, M.; Nakajima, T.; Honda, Y.; Kitao, O.; Nakai, H.; Vreven, T.; Throssell, K.; Montgomery Jr., J. a.; Peralta, J. E.; Ogliaro, F.; Bearpark, M. J.; Heyd, J. J.; Brothers, E. N.; Kudin, K. N.; Staroverov, V. N.; Keith, T. a.; Kobayashi, R.; Normand, J.; Raghavachari, K.; Rendell, a. P.; Burant, J. C.; Iyengar, S. S.; Tomasi, J.; Cossi, M.; Millam, J. M.; Klene, M.; Adamo, C.; Cammi, R.; Ochterski, J. W.; Martin, R. L.; Morokuma, K.; Farkas, O.; Foresman, J. B.; Fox, D. J. Gaussian 16 Revision C.01. Gaussian Inc.: Wallingford CT 2016.

(14) Sedo, G.; Van Wijngaarden, J. Fourier Transform Microwave Spectra of a New Isomer of OCS- CO2. *J. Chem. Phys.* **2009**, *131* (4), 044303.

(15) Evangelisti, L.; Grabowiecki, A.; Van Wijngaarden, J. Chirped Pulse Fourier Transform Microwave Study of 2,2,2-Trifluoroethyl Formate. *J. Phys. Chem. A* **2011**, *115* (30), 8488–8492.

(16) Western, C. M. PGOPHER: A Program for Simulating Rotational, Vibrational and Electronic Spectra. *J. Quant. Spectrosc. Radiat. Transf.* **2017**, *186*, 221–242.

(17) Hartwig, H.; Dreizler, H. The Microwave Spectrum of Trans-2,3-Dimethyloxirane in Torsional Excited States. *Zeitschrift für Naturforsch. A* **1996**, *51* (8), 923–932.

(18) Hansen, N.; Mäder, H.; Bruhn, T. A Molecular Beam Fourier Transform Microwave Study of 0-Tolunitrile: 14N Nuclear Quadrupole Coupling and Methyl Internal Rotation Effects. *Mol. Phys.* **1999**, *97* (4), 587–595.

(19) Kraitchman, J. Determination of Molecular Structure from Microwave Spectroscopic Data. *Am. J. Phys.* **1953**, *21* (1), 17–24.

(20) Kisiel, Z. *PROSPE - Programs for ROtational SPEctroscopy*. http://info.ifpan.edu.pl/~kisiel/prospe.htm (accessed 2020-06-01).

(21) Costain, C. C. Further Comments on the Accuracy of Rs Substitution Structures. *Trans. Am. Crystallogr. Assoc* **1966**, *2*, 157–164.

(22) Demaison, J.; Rudolph, H. D. When Is the Substitution Structure Not Reliable? *J. Mol. Spectrosc.* **2002**, *215* (1), 78–84.

(23) Nguyen, H. V. L.; Kleiner, I. Understanding (Coupled) Large Amplitude Motions: The Interplay of Microwave Spectroscopy, Spectral Modeling, and Quantum Chemistry. *Phys. Sci. Rev.* **2022**, *7* (6), 679–726.

(24) Spangler, L. H. Structural Information from Methyl Internal Rotation Spectroscopy. *Annu. Rev. Phys. Chem.* **1997**, *48* (1), 481–510.

(25) Nguyen, T.; Van, V.; Gutlé, C.; Stahl, W.; Schwell, M.; Kleiner, I.; Nguyen, H. V. L. The

Microwave Spectrum of 2-Methylthiazole: 14N Nuclear Quadrupole Coupling and Methyl Internal Rotation. *J. Chem. Phys.* **2020**, *152* (13), 134306.

Chapter 6 – Conclusions and Future Work

6.1. Summary

The work conducted in this thesis sought to examine molecules of potential astrophysical interest containing methyl internal rotation in the presence of other internal interactions using a combined theoretical and experimental approach. Three molecules were chosen to study this, namely, methyl cyanoacetate (MCA, Chapter 4), 2-methyl-2-oxazoline (2M2O, Chapter 5) and 2-ethyl-2-oxazoline (2E2O, Chapter 5).

Much of the previous work on MCA had centered around its ground state geometry, with a decades-long discrepancy in the literature regarding the orientation of the terminal cyano group with respect to the carbonyl group. In this present work, we were able to conclusively show that the ground state geometry exhibits a *near-anti* orientation of the cyano fragment with respect to the carbonyl, with the oft-attributed *gauche* arrangement representing a transition state between the ground state rotamer and the higher-energy *syn* conformer. This second conformer was not detected in this work, likely a result of the *syn* conformer relaxing to the *near-anti* conformer due to conformational cooling in the supersonic jet. The experimentally derived barrier to internal rotation for the *near-anti* conformer was found to be 4.579(6) kJ mol^{-1}, aligning closely with the barrier predicted at the MP2/aug-cc-pVTZ level of theory (4.50 kJ mol^{-1}) but being nearly twice as large as the barrier predicted using B3LYP-D3(BJ)/aug-cc-pVTZ (2.63 kJ mol^{-1}), which illustrates the known problems with accurately determining barriers based on calculations. This barrier was ~10% smaller than the V_3 barrier for methyl acetate (5.0791(7) kJ mol^{-1})[1], which showed that the increased hyperconjugative effects due to the interactions between the lone pairs of the ester oxygen and the π^* orbitals of the cyano fragment also influenced the V_3 barrier for MCA. This exemplifies a general trend for methyl rotor barriers, wherein an increase in hyperconjugative interactions often results in lower V_3 barrier than in similar molecules without those effects.

These effects were further illustrated through the study of 2M2O and 2E2O, whose rotational spectra were studied for the first time in this work. The V_3 barriers for 2M2O and the ground state conformer of 2E2O were readily determined by analyzing the splitting patterns in the spectra, whereas any splittings due to the methyl rotor for the higher-energy conformer of 2E2O were not resolvable and thus no barrier could be derived. As with MCA, the experimentally derived

V_3 barriers were underestimated by calculations, with the MP2 method generally performing better than B3LYP in the case of both 2M2O and 2E2O-I. The V_3 barriers of 5.3779(4) kJ mol^{-1} and 10.88(6) kJ mol^{-1} for 2M2O and 2E2O-I, respectively, were compared to those of other methylated five-membered heterocycles, where it was found that the barrier heights were in general larger than methyl rotors present on a fully unsaturated ring. This suggested that the loss in hyperconjugative interactions in the partially unsaturated rings in the compounds studied in this work may be responsible for the increase in the barrier, which follows similarly what was observed for MCA (wherein the increase in hyperconjugative interactions resulted in a lower barrier). It was similarly observed that the barriers in molecules with heteroatoms on both sides of the methyl substitution site were lower than those without a heteroatom on either one or both sites. It is hardly surprising, then, that the V_3 barriers in either conformer of 2E2O are much larger, as the methyl substitution site is largely separated from any hyperconjugation as well as the two heteroatoms of the ring. This all illustrates the sensitivity of the barrier heights for internal dynamics of organic molecules to subtle changes in the charge distribution molecules, where even minor changes in structure result in sometimes dramatic differences.

6.2. Future Work

The present work can be extended in a number of ways, as the number of studies on molecules with internal rotation alongside other LAMs is limited. Particularly, further studies on methylated molecules with partially unsaturated rings are warranted to understand how these dynamics intersect. Some immediate examples that would be logical but impactful continuations of the present work would be:

(i) Further exploring the relationship between the position of the methyl on the 2-oxazoline ring. We know from the study of methylated oxazole species[2] that with the methyl group on the 4- or 5-positions on the ring, the barrier heights increase and thus a similar trend would be expected; however, the 4- and 5-positions on 2-oxazoline are both on the flexible part of the ring, and thus more data on how the flexibility affects the V_3 barriers could be surmised.

(ii) Extending the study to methylated 2-thiazoline species. Recently, the spectrum of 2-methylthiazole[3] was studied, where the V_3 barrier was determined to be much lower than that of 2-methyloxazole. Again, a similar effect would be expected in the case of

2-methyl-2-thiazoline when compared with 2M2O, but unlike in the case of 2M2O where the ring puckering is vibrationally averaged, initial calculations predict that the puckering in 2M2T should be explicitly observable, which would allow for the opportunity for more direct inferences into how the flexibility of the molecule is reflected in the internal rotation barriers.

(iii) While not studied as a part of this work, the broadband spectra for 2M2O showed additional transitions that were assigned to a water complex, which itself seemed to have an additional out-of-plane motion due to the positioning of the water molecule relative to the parent species. Studying the effect of complexation on its spectrum could lead to further insights into the 2M2O system in particular.

The above examples would help to lay the groundwork for a broader study on methyl rotors in other partially unsaturated or even fully saturated ring systems, as these have largely gone unstudied as of the writing of this work. Part of the challenge in studying these molecules is that these types of coupled internal motions are difficult to accurately model, and programs being used to analyze molecules containing internal rotors are still in active development.[4,5] These studies could thus highlight areas that are not well captured with the current models and help to improve further iterations of these programs. The spectra of such molecules can be complex, but microwave spectroscopy has proven to be a powerful tool in the interpretation of their spectra. As well, given that methyl rotors have been shown to be highly sensitive to the internal dynamics of the molecular systems they are present in, their study provides an intimate look into how these systems operate.

6.3. References

(1) Nguyen, H. V. L.; Kleiner, I.; Shipman, S. T.; Mae, Y.; Hirose, K.; Hatanaka, S.; Kobayashi, K. Extension of the Measurement, Assignment, and Fit of the Rotational Spectrum of the Two-Top Molecule Methyl Acetate. *J. Mol. Spectrosc.* **2014**, *299*, 17–21.

(2) Fliege, E.; Dreizler, H.; Meyer, M.; Iqbal, K.; Sheridan, J. 14N Nuclear Quadrupole Coupling and Methyl Internal Rotation of 2-, 4-, and 5-Methyl Oxazole. *Zeitschrift für Naturforsch. A* **1986**, *41* (4), 623–636.

(3) Nguyen, T.; Van, V.; Gutlé, C.; Stahl, W.; Schwell, M.; Kleiner, I.; Nguyen, H. V. L. The Microwave Spectrum of 2-Methylthiazole: 14N Nuclear Quadrupole Coupling and Methyl

Internal Rotation. *J. Chem. Phys.* **2020**, *152* (13), 134306.

(4) Kleiner, I. Asymmetric-Top Molecules Containing One Methyl-like Internal Rotor: Methods and Codes for Fitting and Predicting Spectra. *J. Mol. Spectrosc.* **2010**, *260* (1), 1–18.

(5) Nguyen, H. V. L.; Kleiner, I. Understanding (Coupled) Large Amplitude Motions: The Interplay of Microwave Spectroscopy, Spectral Modeling, and Quantum Chemistry. *Phys. Sci. Rev.* **2022**, *7* (6), 679–726.